AIAA Meeting Papers on Disc, January 1997
A9715767, F49620-94-1-0019, F49620-95-1-0405, AIAA Paper 97-0755

Direct numerical simulation of hypersonic boundary-layer transition over blunt leading edges. I - A new numerical method and validation

Xiaolin Zhong
California Univ., Los Angeles

AIAA, Aerospace Sciences Meeting & Exhibit, 35th, Reno, NV, Jan. 6-9, 1997

This paper presents and tests a new high-order upwind finite difference shock fitting method for the direct simulations of hypersonic flows with strong bow shocks. There are three main aspects of the new method: a simple unsteady shock fitting formulation, new upwind high-order finite difference schemes for spatial discretization, and new third-order semi-implicit Runge-Kutta schemes for temporal discretization. The results of accuracy tests of the new fifth-order shock-fitting method are presented for four test cases: 1D wave equation, 2D direct numerical simulation (DNS) of stability of supersonic Couette flow, steady viscous hypersonic flow over a circular cylinder, and the DNS of receptivity to freestream acoustic disturbances for hypersonic boundary layers over a parabola. (Author)

Direct Numerical Simulation of Hypersonic Boundary-Layer Transition Over Blunt Leading Edges, Part I: A New Numerical Method and Validation

Xiaolin Zhong *
University of California, Los Angeles, California 90095

Abstract

Direct numerical simulation (DNS) of the stability and transition of hypersonic boundary layers over blunt leading edges requires high-order accurate numerical methods to resolve a wide range of time and length scales. In addition, numerical methods for such simulation need to resolve unsteady bow shock motion and shock/disturbance interaction accurately. This paper presents and tests a new high-order upwind finite difference shock fitting method for the direct simulations of hypersonic flows with strong bow shocks. There are three main aspects of the new method: a simple unsteady shock fitting formulation, new upwind high-order finite difference schemes for spatial discretization, and new third-order semi-implicit Runge-Kutta schemes for temporal discretization. The results of accuracy tests of the new fifth-order shock-fitting method are presented in this paper for four test cases: 1-D wave equation, 2-D DNS of stability of supersonic Couette flow, steady viscous hypersonic flow over a circular cylinder, and finally, the DNS of receptivity to freestream acoustic disturbances for hypersonic boundary layers over a parabola.

Introduction

The prediction of laminar-turbulent transition in hypersonic boundary layers is a critical part of the aerodynamic design and control of advanced hypersonic vehicles [1,2]. Recently, direct numerical simulation has become a powerful tool in the study of fundamental flow physics of the stability and transition of boundary layers [3,4]. The direct numerical simulation approach studies the transitional boundary layers [3] by numerically solving the time-dependent three-dimensional Navier-Stokes equations for the temporally or spatially evolving instability waves. Such simulation requires that all relevant flow time and length scales are resolved by the numerical solutions using highly accurate numerical methods.

*Assistant Professor, Mechanical and Aerospace Engineering Department, Member AIAA.

Most DNS work on boundary layer transition are for incompressible flows [5–14]. The DNS of compressible boundary layer transition has occurred only in the last few years. Erlebacher et al. [15,16] studied the secondary instability mechanism of compressible boundary layers over a flat plate by temporal and spatial direct numerical simulations. Thumm et al. [17], Fasel et al. [18], and Eibler et al. [19,20] performed spatial DNS of the oblique breakdown of transition in a supersonic boundary layer over a flat plate. Adams and Kleiser [21,22] studied the subharmonic transition process of a flat-plate at a freestream Mach number of 4.5 by temporal direct numerical simulation. This work was extended to spatial DNS of a flat-plate boundary layer of Mach 1.6 to 4.5 by Guo et al. [23] in the same research group. Pruett and Zang [24] conducted temporal DNS studies of laminar breakdown in high-speed axisymmetric boundary layers over a hollow cylinder and a sharp cone. Pruett et al. [25–27] then performed spatial simulations for supersonic boundary layers over flat plates and sharp cones. These DNS studies of compressible boundary layers show that the DNS of high-speed boundary transition is feasible on existing computers using efficient and accurate numerical methods. So far, DNS studies of compressible boundary layers have been limited to perfect gas flows over simple flat body surfaces without the presence of shock waves.

This paper is concerned with numerical methods for the DNS of stability and transition of hypersonic boundary layers behind blunt bodies (Fig. 1). For the DNS of such flows, it is difficult to apply the existing methods due to the lack of efficient semi-implicit numerical methods for compressible viscous flows, presence of shock waves, and the stiffness of the equations in reacting hypersonic flows. This paper presents a new high-order (fifth and sixth order) upwind finite difference shock fitting method for the direct simulation of hypersonic flows with a strong bow shock and with stiff source terms. There are three main aspects of the new method for hypersonic flow DNS: a new shock fitting formulation, new upwind high-order finite difference schemes, and third-order semi-implicit Runge-Kutta schemes recently derived [28].

First, a shock fitting formulation, which is very simple for the high-order discretization in three-

dimensional shock fitting calculations with unsteady shock motion, is presented in this paper. The use of shock fitting method makes it possible to use high-order linear schemes for spatial discretization of the flow equations behind the bow shock. Hussaini, Kopriva, Salas, and Zang [29] used the shock fitting spectral method to simulate shock/turbulent interaction. Recently, Cai [30] used a shock fitting method to compute two-dimensional detonation waves. This paper presents a simple formulation for shock fitting calculation of three-dimensional unsteady hypersonic flows. The current formulation is simple because the perturbation relation across the shock is consistent with conservative flux and its Jacobian used in the conservation equations. As a result, high-order schemes can be applied to the shock fitting calculations easily.

Second, new upwind compact and explicit high-order finite difference schemes derived in a recent paper [31] are used in computing inviscid fluxes. Most finite difference methods used in direct numerical simulations have been central difference schemes [26,32,33] containing only phase errors without any numerical dissipation errors. However, high-order central schemes are often not robust enough for convection dominated problems. Extra filtering procedures, which are equivalent to adding numerical dissipation, are often required to control the aliasing errors and to stabilize the computations. In addition, central difference schemes of fourth order or higher are often unstable when they are coupled with high-order boundary schemes using simple one-sided finite difference approximations [26,34,35]. Boundary closure schemes, which are needed because of wide grid stencils of high-order inner schemes, often determine the overall accuracy of the computations using high-order inner schemes. For a global scheme of p-th order [36], the boundary schemes have to be at least p-1-th order. Carpenter, Gottlieb, and Abarbanel [34,35] showed that for a sixth-order inner central compact scheme, only a third-order boundary scheme can be used without introducing instability. The resulting stable 3,4-6-4,3 compact scheme, which denotes a sixth-order inner scheme with third and fourth order boundary schemes at the first and second boundary points respectively [35], is fourth order globally accurate even though the inner scheme is sixth-order accurate. On the other hand, Rai and Moin [37] showed that modern upwind schemes are very robust even when they are made high-order accurate. Ref. [37] used a spatially fifth-order upwind-bias explicit finite difference scheme for solving the Navier-Stokes equations. The implicit numerical dissipation in the upwind-bias schemes is enough to control the aliasing errors. In recent years, many other upwind high-order schemes have also been developed [38–41] for the direct numerical simulation of transitional and turbulent boundary layers or other flows.

The upwind schemes presented in [31] use central grid stencils with built-in implicit numerical dissipation, similar to the fifth-order explicit upwind scheme of Zingg et al. [40] and the 4th-order compact upwind schemes of Adams and Shariff [41]. The current upwind schemes, which include both upwind compact and explicit schemes, are more general and systematic in derivation and analysis. The orders of accuracy of the current upwind schemes are one-order lower than the maximum orders the central stencils can achieve. Each upwind scheme contains an adjustable coefficient in the leading dissipative truncation term. The free parameter is chosen so that the upwind schemes do not have excessive numerical dissipation in the simulations and the inner schemes are stable when they are coupled with high-order numerical boundary schemes. The dissipation errors of the schemes are set to be smaller or comparable to the phase errors for well resolved low wavenumber modes and to damp out unresolved higher wavenumber modes. For the stability of the high-order inner schemes with boundary schemes, asymptotic stability of the schemes is analyzed by computing the eigenvalue spectrums of spatial approximations with boundary schemes. It is found that the high-order upwind schemes help to stabilize the overall schemes when they are coupled with high-order boundary closures.

Third, the time advancement of the governing equations with stiff viscous terms in the boundary layer or thermo-chemical nonequilibrium source terms is solved by third-order semi-implicit Runge-Kutta schemes [42,43]. The third-order semi-implicit Runge-Kutta schemes are able to compute stiff reactive flow equations with third-order temporal accuracy, and They are unconditionally stable for the stiff terms when the non-stiff terms satisfy explicit stability conditions for the Runge-Kutta schemes.

Governing Equations

Though real gas effects become important as gas temperature increases [44] for hypersonic flow behind a strong bow shock, perfect gas assumption is used in this paper. The method can be extended to nonequilibrium real-gas flow if necessary. The governing equations are the unsteady three-dimensional Navier-Stokes equations:

$$\frac{\partial U}{\partial t} + \frac{\partial F_j}{\partial x_j} + \frac{\partial F_{vj}}{\partial x_j} = 0 \qquad (1)$$

where

$$U = \{\rho,\ \rho u_1,\ \rho u_2,\ \rho u_3,\ e\} \tag{2}$$

$$F_j = = \begin{Bmatrix} \rho u_j \\ \rho u_1 u_j + p\delta_{1j} \\ \rho u_2 u_j + p\delta_{2j} \\ \rho u_3 u_j + p\delta_{3j} \\ (e+p)\,u_j \end{Bmatrix} \tag{3}$$

$$F_{vj} = \begin{Bmatrix} 0 \\ \tau_{1j} \\ \tau_{2j} \\ \tau_{3j} \\ \tau_{jk}u_k - q_j \end{Bmatrix} \tag{4}$$

$$p = \rho RT \tag{5}$$

$$e = \rho(c_v T + \frac{\rho}{2} u_k u_k) \tag{6}$$

$$\tau_{ij} = -\mu\left(\frac{\partial u_i}{\partial x_j} + \frac{\partial u_j}{\partial x_i}\right) + 2\mu/3\frac{\partial u_k}{\partial x_k}\delta_{ij} \tag{7}$$

$$q_j = -\kappa\frac{\partial T}{\partial x_j} \tag{8}$$

A shock fitting method is used to solve unsteady three-dimensional viscous hypersonic flow over a wedge shown in Figure 2. The general curvilinear three-dimensional coordinates (ξ, η, ζ, τ) are used along the body fitted grid lines (Fig. 2). Shock fitting methods are used to treat the bow shock as a computational boundary. The transient movement of the shock and its interaction with disturbance waves are solved as part of the solutions. Therefore, the grid surface of η = constant is unsteady due to the shock movement, but the grid surfaces of ξ = constant and ζ = constant are fixed plane surfaces during the calculations. In particular, the ξ = constant surfaces are generated such that they are normal to the wall surface. Therefore, only the η = constant grid lines change when the bow shock moves.

The transformation relations for the current grid systems are

$$\begin{cases} \xi = \xi(x,y,z) \\ \eta = \eta(x,y,z,t) \\ \zeta = \zeta(x,y,z) \\ \tau = t \end{cases} \iff \begin{cases} x = x(\xi,\eta,\zeta,\tau) \\ y = y(\xi,\eta,\zeta,\tau) \\ y = y(\xi,\eta,\zeta,\tau) \\ t = \tau \end{cases} \tag{9}$$

where $\xi_t = 0$ and $\zeta_t = 0$ because the ξ and ζ grid lines are fixed when the shock boundary moves.

In the numerical simulations, the governing equation (1) are transformed into the computational domain (ξ, η, ζ, τ) as follows

$$\frac{1}{J}\frac{\partial U}{\partial \tau} + \frac{\partial E'}{\partial \xi} + \frac{\partial F'}{\partial \eta} + \frac{\partial G'}{\partial \zeta} + \frac{\partial E'_v}{\partial \xi} + \frac{\partial F'_v}{\partial \eta} + \frac{\partial G'_v}{\partial \zeta} + U\frac{\partial(\frac{1}{J})}{\partial \tau} = \frac{W}{J} \tag{10}$$

where

$$E' = \frac{F_1\xi_x + F_2\xi_y + F_3\xi_z}{J} \tag{11}$$

$$F' = \frac{F_1\eta_x + F_2\eta_y + F_3\eta_z + U\eta_t}{J} \tag{12}$$

$$G' = \frac{F_1\zeta_x + F_2\zeta_y + F_3\zeta_z}{J} \tag{13}$$

$$E'_v = \frac{F_{v1}\xi_x + F_{v2}\xi_y + F_{v3}\xi_z}{J} \tag{14}$$

$$F'_v = \frac{F_{v1}\eta_x + F_{v2}\eta_y + F_{v3}\eta_z}{J} \tag{15}$$

$$G'_v = \frac{F_{v1}\zeta_x + F_{v2}\zeta_y + F_{v3}\zeta_z}{J} \tag{16}$$

where J is the Jacobian of the coordinate transformation, and ξ_x, ξ_y, ξ_z, η_x, η_y, η_z, η_t, ζ_x, ζ_y, and ζ_z are the grid transformation metrics, which are computed as functions of the body shape, the grid-point distribution along the grid lines, the wall-normal distance $H(\xi,\zeta,\tau)$ between the shock and the wall along the η grid lines (see Fig. 2), and the time derivative H_τ. These metrics functions are functions of time through H and H_τ.

The governing equations are discretized in the uniform computational space. In the equations, the transformed inviscid fluxes E', F', and G' are standard flux terms with known eigenvalues and eigenvectors. The transport flux terms E'_v, F'_v, and G'_v contain first-order spatial derivatives of velocity and temperature. These derivatives in the Cartesian coordinates (x,y,z) are transformed into the computational coordinates (ξ,η,ζ) using a chain rule for spatial discretization.

A Simple Shock Fitting Formulation

The shock fitting method treats the bow shock as a computational boundary at $\eta = \eta_{\max}$ as

$$\eta(x,y,z,t) = \eta_{\max} = \text{constant} \tag{17}$$

The flow variables behind the shock are determined by the Rankine-Hugoniot relation across the shock and a

characteristic compatibility equation from behind the shock. As shown in Fig. 2, the position and velocity of the shock front are functions of $H(\xi,\zeta,\tau)$ and $H_\tau(\xi,\zeta,\tau)$, which are solved as unknown variables using high-order finite difference methods. A simple formulation for the governing equations for the shock movement is derived in the section. The method is similar to that used by Cai [30], but is simplier in obtaining the shock equations by using the same metrics and flux Jacobian as those used in discretization of interior governing equations.

The normal vector of the shock front is

$$\mathbf{n} = \frac{\eta_x \mathbf{i} + \eta_y \mathbf{j} + \eta_z \mathbf{k}}{|\nabla \eta|} \tag{18}$$

and the velocity of the shock front in the direction of $\mathbf{n}$ is

$$v_n = -\frac{\eta_t}{|\nabla \eta|} \tag{19}$$

where $|\nabla \eta| = \sqrt{\eta_x^2 + \eta_y^2 + \eta_z^2}$.

The flow variables across the shock are governed by the Rankine-Hugonoit conditions:

$$F'_s = F'_0 \tag{20}$$

where the subscript s represents the variable immediately behind the shock and subscript 0 represents the variable on the free stream side of the shock surface. The flux F', which is the flux in the computational space along the η grids line, is given by Eq. (12) as

$$F' = \frac{F_1\eta_x + F_2\eta_y + F_3\eta_z + U\eta_t}{J} \tag{21}$$

$$= \frac{|\nabla \eta|}{J}(\mathbf{F}\cdot\mathbf{n} - v_n U) \tag{22}$$

where

$$\mathbf{F} = F_1\mathbf{i} + F_2\mathbf{j} + F_3\mathbf{k} \tag{23}$$

The Rankine-Hugoniot relations lead to jump conditions for flow variables behind the shock as functions of U_0 and the grid velocity v_n, i.e.,

$$p_s = p_0\left[1 + \frac{2\gamma}{\gamma+1}(M_{n0}^2 - 1)\right] \tag{24}$$

$$\rho_s = \rho_0\left[1 + \frac{(\gamma+1)M_{n0}^2}{(\gamma-1)M_{n0}^2 + 2}\right] \tag{25}$$

$$u_{ns} = v_n + \frac{\rho_0}{\rho_s}(u_{n0} - v_n) \tag{26}$$

$$\mathbf{u}_{ts} = \mathbf{u}_{t0} = \mathbf{u}_0 - u_{n0}\mathbf{n} \tag{27}$$

$$\mathbf{u}_s = \mathbf{u}_{ts} + u_{ns}\mathbf{n} = \mathbf{u}_0 + (u_{ns} - u_{n0})\mathbf{n} \tag{28}$$

where M_{n0} is the normal component of the incoming Mach number relative to the shock based on the speed of sound, $\mathbf{u}$ is the velocity vector, $\mathbf{u_t}$ is the tangential velocity vector, u_n is the normal velocity component. The definitions for these variables are

$$M_{n0} = \frac{u_{n0} - v_n}{c_0} \tag{29}$$

$$u_n = \mathbf{u}\cdot\mathbf{n} \tag{30}$$

$$\mathbf{u}_t = \mathbf{u} - u_n\mathbf{n} \tag{31}$$

In order to compute the flow variable behind the shock using the shock jump conditions above, the velocity of the shock front v_n is needed. The shock normal velocity is computed by a characteristic relation behind the shock.

In order to solve the shock movement, a characteristic compatibility equation at the grid point immediately behind the shock is needed. It is found that the shock fitting computations and the shock geometry transformation relations are greatly simplified if we derive the characteristic compatibility equation in the conservation-law form, which can de derived directly from Eq. (1) in the direction along the η coordinates. Specifically, the interior equation (1) in the computational domain at the point immediately behind the shock front can be written as:

$$\frac{1}{J}\frac{\partial U}{\partial \tau} + \frac{\partial F'}{\partial \eta} = \left(\frac{W}{J} - \frac{\partial E'}{\partial \xi} - \frac{\partial G'}{\partial \zeta} - \frac{\partial E'_v}{\partial \xi} - \frac{\partial F'_v}{\partial \eta} - \frac{\partial G'_v}{\partial \zeta} + U\frac{\partial(\frac{1}{J})}{\partial \tau}\right) \tag{32}$$

where the equation is evaluated at point s behind the shock. In the equations, the Jacobian matrix, $B'_s = (\partial F'/\partial U)_s$, has the following eigenvalues:

$$\frac{|\nabla\eta|}{J}(u_n - v_n)_s, \quad \cdots, \quad \frac{|\nabla\eta|}{J}(u_n - v_n)_s, \quad \frac{|\nabla\eta|}{J}(u_n - v_n - c)_s, \quad \frac{|\nabla\eta|}{J}(u_n - v_n + c)_s \tag{33}$$

The corresponding left eigenvectors are

$$\mathbf{l}_1, \ \mathbf{l}_2, \ \cdots, \ \mathbf{l}_{N-1}, \ \mathbf{l}_N \tag{34}$$

where N is the number of independent variables in the equations. Specifically, the left eigenvector $\mathbf{l_N}$ is [45]

$$\mathbf{l_N} = \frac{1}{c^2}\begin{bmatrix} \frac{\kappa}{2}\mathbf{u}\cdot\mathbf{u} - cu_n \\ -(\frac{1}{2}cn_x - \frac{\kappa}{2}u) \\ -(\frac{1}{2}cn_y - \frac{\kappa}{2}v) \\ -(\frac{1}{2}cn_z - \frac{\kappa}{2}w) \\ \frac{\kappa}{2} \end{bmatrix}_s \quad (35)$$

where

$$c = \sqrt{\gamma\frac{p}{\rho}} \quad (36)$$

$$\kappa = \gamma - 1 \quad (37)$$

By definition, the left eigenvector behind the shock satisfies:

$$\mathbf{l_N}\cdot B'_s = \frac{|\nabla\eta|}{J}(u_n - v_n + c)_s\,\mathbf{l_N} \quad (38)$$

The characteristic field approaching the shock from behind corresponds to the eigenvalue of $\frac{|\nabla\eta|}{J}(u_n - v_n + c)_s$. The compatibility relation for this characteristic field can be obtained by multiplying Eq. (32) by $\mathbf{l_N}$,

$$\mathbf{l_N}\cdot\left(\frac{\partial U}{\partial\tau}\right) = \mathbf{l_N}\cdot\left(\frac{W}{J} - \frac{\partial E'}{\partial\xi} - \frac{\partial F'}{\partial\eta} - \frac{\partial G'}{\partial\zeta} - \frac{\partial F_v}{\partial\xi} - \frac{\partial F_v}{\partial\eta} - \frac{\partial F_v}{\partial\zeta} + U\frac{\partial(\frac{1}{J})}{\partial\tau}\right)J \quad (39)$$

On the other hand, the shock jump condition (20) can be rewritten as

$$[F'] = (\mathbf{F_s} - \mathbf{F_0})\cdot\mathbf{a} + (U_s - U_0)\,b = 0 \quad (40)$$

where

$$\mathbf{a} = (\frac{\eta_x}{J})_s\mathbf{i} + (\frac{\eta_y}{J})_s\mathbf{j} + (\frac{\eta_z}{J})_s\mathbf{k} \quad (41)$$

$$b = (\frac{\eta_t}{J})_s. \quad (42)$$

Taking derivative of Eq. (40) with respective to τ in the computational space leads to

$$B'_s\frac{\partial U_s}{\partial\tau} - B'_0\frac{\partial U_0}{\partial\tau} + (\mathbf{F_s} - \mathbf{F_0})\cdot\frac{\partial\mathbf{a}}{\partial\tau} + (U_s - U_0)\frac{\partial b}{\partial\tau} = 0 \quad (43)$$

where the flux Jacobian

$$B' = \frac{\partial F'}{\partial U} \quad (44)$$

is the Jacobian of the η direction flux defined in the conservation equations (10), and

$$\frac{\partial\mathbf{a}}{\partial\tau} = \frac{\partial(\frac{\eta_x}{J})_s}{\partial\tau}\mathbf{i} + \frac{\partial(\frac{\eta_y}{J})_s}{\partial\tau}\mathbf{j} + \frac{\partial(\frac{\eta_z}{J})_s}{\partial\tau}\mathbf{k} \quad (45)$$

$$\frac{\partial b}{\partial\tau} = \frac{\partial(\eta_\tau/J)_s}{\partial\tau} \quad (46)$$

These time derivatives of the grid metrics can be derived by the same methods as those used in discretization of the interior equations.

Finally, the equation for the shock velocity can be obtained by multiplying both sides of Eq. (43) by $\mathbf{l_N}$ and using the relation of (38), i.e.,

$$\frac{\partial b}{\partial\tau} = \frac{-1}{[\mathbf{l_N}\cdot(U_s - U_0)]}\left[\frac{|\nabla\eta|}{J}(u_n - v_n + c)_s\,\mathbf{l_N}\cdot(\frac{\partial U}{\partial\tau})_s + \mathbf{l_N}\cdot(\mathbf{F_s} - \mathbf{F_0})\cdot\frac{\partial\mathbf{a}}{\partial\tau} - (\mathbf{l_N}\cdot\mathbf{B'_0})\frac{\partial U_0}{\partial\tau}\right] \quad (47)$$

where the term $\mathbf{l_N}\cdot\frac{\partial U_s}{\partial\tau}$ is computed using the characteristic relation (39), in which the spatial derivatives are discretized together with the discretization of the interior points for the Eq. (10) using the same schemes at the interior algorithm applied to boundary behind the shock. In the equation above, $\frac{\partial b}{\partial\tau}$ and $\frac{\partial\mathbf{a}}{\partial\tau}$ can be expressed as function of H and H_τ as follows

$$\frac{\partial b}{\partial\tau} = d_1(\xi,\zeta,H,H_\tau) + d_2(\xi,\zeta,H,H_\tau)\frac{\partial H_\tau}{\partial\tau} \quad (48)$$

$$\frac{\partial\mathbf{a}}{\partial\tau} = \mathbf{d}(\xi,\zeta,H,H_\tau) \quad (49)$$

The coefficients, d_1, d_2, and vector $\mathbf{g}$ are functions of grid metrics.

Therefore, the equation for the shock acceleration can be obtained from Eqs. (48) to (49) in the following form:

$$\frac{\partial H_\tau}{\partial\tau} = f\left(\xi,\ \zeta,\ U_s,\ \mathbf{l_{N-1}}\cdot(\frac{\partial U}{\partial\tau})_s,\ U_0,\ \frac{\partial U_0}{\partial\tau},\ H,\ H_\tau\right) \quad (50)$$

$$\frac{\partial H}{\partial \tau} = H_\tau \tag{51}$$

The two equations above describe the shock normal velocity and shock shape, and they can be integrated in time simultaneously with the interior flow variables using Runge-Kutta methods. After the values of H and H_τ are determined, the flow variables behind the shock can be computed by the jump conditions across the shock using Eqs. (24) to (28). The grids and metrics are modified according to the new values of H and H_τ.

The current formulation is simple because the governing equations for the shock movement are derived using conservative variable and flux Jacobian in Eq. (43) using the relation (38). The same discretization of the interior governing equations is used to evaluate $\mathbf{l}_N \cdot (\frac{\partial U_s}{\partial \tau})_s$ at grid points immediately behind the shock. In addition, all geometric definitions of the shock front are the same as the grid metrics used in the interior equation transformation, which are stored in the computer. In doing so, the current approach avoids complication of using the non-conservation variables and locally defined geometric parameters for the shock front in deriving the time derivatives of the shock jump condition.

High-Order Upwind Schemes for Spatial Discretization

The governing equation (10) is discretized in the computational domain (ξ, η, ζ, τ) using the method of lines. Because there is no shock in the computational domain, high-order finite difference methods are used for spatial discretization of the equations, where the inviscid and viscous flux terms are discretized using different methods: central difference schemes for the viscous flux terms and upwind schemes for the inviscid flux terms.

In Ref. [31], a family of finite-difference upwind schemes of third, fifth, and seventh orders have been derived for the direct numerical simulations of hypersonic boundary layers. Either compact or non-compact (explicit) schemes can be used. Each upwind scheme uses a central stencil with a free damping parameter α, which is chosen such that the inner scheme is stable when it is coupled with high-order numerical boundary schemes and the dissipation errors are smaller or comparable to phase errors. These high-order upwind schemes are used for the spatial discretization in the shock-fitting algorithm.

The upwind schemes are described using the one-dimensional linear wave equation:

$$\frac{\partial u}{\partial t} + c\frac{\partial u}{\partial x} = 0 \qquad a \le x \le b \tag{52}$$

where $c > 0$. The downwind algorithm for negative c can be derived similarly.

The linear wave equation (52) is solved by the method of lines, where the spatial derivative, $\partial u/\partial x$, is first discretized in space while keeping the temporal derivative in the equations. The general finite-difference approximation for $\partial u/\partial x$ located at i-th grid point can be written as [32,41]

$$\sum_{k=-M+M_0+1}^{M_0} b_{i+k}\, u'_{i+k} = \frac{1}{h} \sum_{k=-N+N_0+1}^{N_0} a_{i+k}\, u_{i+k} \tag{53}$$

where uniform grids with grid spacing of h are assumed, and u'_{i+k} is the numerical approximation of $\partial u/\partial x$ located at $(i+k)$-th grid point. On the right hand side of the equation, a total of N grid points are used for u_{i+k} with N_0 points bias with respect to the based point i. A similar grid combination of M and M_0 is used for u'_{i+k} on the left hand side of the equation. In this paper, a scheme using this grid combination is termed the N-N_0-M-M_0 scheme, which includes both compact and explicit schemes as its special cases. For example, the schemes are compact finite difference schemes when $M \ge 2$, and they are explicit finite difference schemes when $M = 1$ and $M_0 = 0$.

Ref. [31] considered a family of upwind compact and explicit high-order finite difference methods using central grid stencils, i.e.,

$$N = 2N_0 + 1 \tag{54}$$
$$M = 2M_0 + 1 \tag{55}$$

The coefficients a_{i+k} and b_{i+k} of the upwind schemes are determined such that the order of the schemes is one order lower than the maximum achievable order for the central stencil, i.e, the orders of the upwind schemes are always odd integers of $p = 2(N_0 + M_0) - 1$. As a result, there is a free parameter α in the coefficients a_{i+k} and b_{i+k}. The free parameter is set to be the coefficient of the leading truncation term which is a

derivative even order, i.e.,

$$\sum_{k=-M_0}^{M_0} b_{i+k}\, u'_{i+k} = \frac{1}{h}\sum_{k=-N_0}^{N_0} a_{i+k}\, u_{i+k} - \frac{\alpha}{(p+1)!}h^p\left(\frac{\partial u^{p+1}}{\partial^{p+1}x}\right)_i + \cdots \qquad (56)$$

where $p = 2(N_0+M_0)-1$, and α is the free parameter. All schemes with nonzero α are p-th order accurate, and they are central schemes of $(p+1)$-th order when $\alpha = 0$. The choice of α is not unique, and it has effects mainly on the magnitudes of numerical dissipation. The specific value of α for an upwind scheme is chosen to be large enough to stabilize the high-order upwind inner scheme when it is coupled with stable boundary closure schemes, and to be small enough so that the dissipation errors are comparable to the dispersion errors of the inner scheme.

The detailed expressions of the upwind compact and explicit upwind schemes of fifth and seventh orders are given below. Ref. [31] chose a set of "recommended" values of α based on the accuracy and stability analysis. Since compact schemes with large M involve costly solutions of linear equations in computing derivatives, we are mainly interested in three-point compact schemes ($M = 3$). The third-order compact and explicit upwinds schemes and the upwind seventh-order five-point compact schemes with a 5-2-5-2 stencil are given in [31].

Fifth-Order Upwind Compact Schemes:

$$b_{i-1}\, u'_{i-1} + b_i\, u'_i + b_{i+1}\, u'_{i+1} = \frac{1}{h}\sum_{k=-2}^{2} a_{i+k}\, u_{i+k} - \frac{\alpha}{6!}h^5\left(\frac{\partial u^6}{\partial^6 x}\right)_i + \cdots \qquad (57)$$

where

$$\begin{array}{llll} a_{i+2} = \frac{5}{3}+\frac{5}{6}\alpha & & b_{i+1} = 20+5\alpha \\ a_{i+1} = \frac{140}{3}+\frac{20}{3}\alpha & & b_i = 60 \\ a_i = 0-15\alpha & & b_{i-1} = 20-5\alpha \\ a_{i-1} = -\frac{140}{3}+\frac{20}{3}\alpha & & \\ a_{i-2} = -\frac{5}{3}+\frac{5}{6}\alpha & & \end{array}$$

These 5-2-3-1 schemes are fifth-order upwind compact schemes when $\alpha < 0$, and they reduce to the sixth-order central compact scheme when $\alpha = 0$. The recommended value for α is $\alpha = -1$, which corresponds to the following fifth-order upwind compact inner scheme:

$$25u'_{i-1} + 60u'_i + 15u'_{i+1} = \frac{1}{h}\left(-\frac{5}{2}u_{i-2} - \frac{160}{3}u_{i-1} + 15u_i + 40u_{i+1} + \frac{5}{6}u_{i+2}\right) \qquad (58)$$

Fifth-Order Upwind Explicit Schemes:

$$u'_i = \frac{1}{h\, b_i}\sum_{k=-3}^{3} a_{i+k}\, u_{i+k} - \frac{\alpha}{6!\, b_i}h^5\left(\frac{\partial u^6}{\partial^6 x}\right)_i + \cdots \qquad (59)$$

where

$$\begin{array}{llll} a_{i\pm3} = \pm1+\frac{1}{12}\alpha & & & \\ a_{i\pm2} = \mp9-\frac{1}{2}\alpha & & & \\ a_{i\pm1} = \pm45+\frac{5}{4}\alpha & & & \\ a_i = 0-\frac{5}{3}\alpha & & b_i = 60 & \end{array}$$

These 7-3-1-0 schemes are fifth-order upwind scheme when $\alpha < 0$, and they are sixth-order central scheme when $\alpha = 0$. The recommended value for α is $\alpha = -6$, and the corresponding fifth-order upwind explicit inner scheme is

$$u'_i = \frac{1}{60h}\left(-\frac{3}{2}u_{i-3} + 12u_{i-2} - \frac{105}{2}u_{i-1} + 10u_i + \frac{75}{2}u_{i+1} - 6u_{i+2} + \frac{1}{2}u_{i+3}\right) \qquad (60)$$

It is noted that the fifth-order upwind bias scheme of Rai and Moin [9] is a special case of the current 5th-order upwind schemes corresponding to $\alpha = -12$ and $a_{i+3} = 0$. The stencil of the scheme becomes upwind-bias (6-2-1-0). The recommended upwind scheme above has less numerical dissipation because of smaller α.

Seventh-Order Upwind Compact Schemes:

$$b_{i-1}\, u'_{i-1} + b_i\, u'_i + b_{i+1}\, u'_{i+1} = \frac{1}{h}\sum_{k=-3}^{3} a_{i+k}\, u_{i+k} - \frac{\alpha}{8!}h^7\left(\frac{\partial u^8}{\partial^8 x}\right)_i + \cdots \qquad (61)$$

where

$$
\begin{array}{lcllcl}
a_{i+3} &=& -\frac{1}{8}+\frac{1}{96}\alpha & & & \\
a_{i+2} &=& 3-\frac{1}{6}\alpha & & & \\
a_{i+1} &=& \frac{375}{8}-\frac{65}{96}\alpha & b_{i+1} &=& \frac{45}{2}-\frac{5}{8}\alpha \\
a_i &=& 0+\frac{5}{3}\alpha & b_i &=& 60 \\
a_{i-1} &=& -\frac{375}{8}-\frac{65}{96}\alpha & b_{i-1} &=& \frac{45}{2}+\frac{5}{8}\alpha \\
a_{i-2} &=& -3-\frac{1}{6}\alpha & & & \\
a_{i-3} &=& \frac{1}{8}+\frac{1}{96}\alpha & & &
\end{array}
$$

These 7-3-3-1 schemes are seventh-order upwind compact schemes when $\alpha > 0$, and they are eighth-order central compact scheme when $\alpha = 0$. The recommended value for α is $\alpha = 36$, and the corresponding seventh-order upwind compact inner scheme is

$$
45u'_{i-1}+60u'_i=\frac{1}{h}\left(\frac{1}{2}u_{i-3}-9u_{i-2}\right.
$$
$$
\left.-\frac{285}{4}u_{i-1}+60u_i+\frac{45}{2}u_{i+1}-3u_{i+2}+\frac{1}{4}u_{i+3}\right) \quad (62)
$$

Seventh-Order Upwind Explicit Schemes:

$$
u'_i = \frac{1}{h\,b_i}\sum_{k=-4}^{4} a_{i+k}\,u_{i+k} - \frac{\alpha}{8!\,b_i}h^7\left(\frac{\partial u^8}{\partial^8 x}\right)_i+\cdots \quad (63)
$$

where

$$
\begin{array}{lcllcl}
a_{i\pm4} &=& \mp\frac{3}{14}+\frac{1}{672}\alpha & & & \\
a_{i\pm3} &=& \pm\frac{16}{7}-\frac{1}{84}\alpha & & & \\
a_{i\pm2} &=& \mp 12+\frac{1}{24}\alpha & & & \\
a_{i\pm1} &=& \pm 48-\frac{1}{12}\alpha & & & \\
a_i &=& 0+\frac{5}{48}\alpha & b_i &=& 60
\end{array}
$$

These 9-4-1-0 schemes are seventh-order upwind explicit schemes when $\alpha > 0$, and they are eighth-order central explicit scheme when $\alpha = 0$. The recommended value for α is $\alpha = 36$, and the corresponding seventh-order upwind explicit inner scheme is

$$
u'_i = \frac{1}{60h}\left(\frac{15}{56}u_{i-4}-\frac{19}{7}u_{i-3}+\frac{27}{2}u_{i-2}\right.
$$
$$
-51u_{i-1}+\frac{15}{4}u_i+45u_{i+1}-\frac{21}{2}u_{i+2}
$$
$$
\left.+\frac{13}{7}u_{i+3}-\frac{9}{56}u_{i+4}\right) \quad (64)
$$

Numerical Boundary Schemes

High-order finite difference schemes require additional numerical boundary schemes at grid points near the boundaries of the computational domain. For a p-th order interior scheme, the accuracy of boundary schemes can be $(p-1)$-th order accurate without reducing the global accuracy of the interior scheme. For example, for the fifth-order inner upwind compact scheme given by Eq. (58), two boundary schemes are needed at grid point at $i = 0$, 1, and $i = N-1$, N. It is desirable that the boundary schemes are at least fourth-order so that overall schemes are fifth-order accurate. Both one-sided compact and explicit finite difference schemes can be used as numerical boundary schemes. The expressions of the boundary schemes of up to sixth order can be found in [31]. The orders of accuracies for stable overall schemes when they are coupled with high-order interior schemes were analyzed in [31] and are summerized in Table 3, where the notation of 3,4-6-4,3 denoted by Carpenter et al. as a sixth-order inner scheme with third and fourth order boundary schemes at the first and second boundary points respectively [35].

Discretization of Inviscid Flux Vectors

For the inviscid flux vector in the governing equation (10), the flux Jacobians contains both positive and negative eigenvalues in general. In this paper, a simple local Lax-Friedrichs scheme is used to split the inviscid flux vectors into positive and negative wave fields. For example, the flux term E' in Eq. (10) can be split into two terms of pure positive and negative eigenvalues as follows

$$
E' = E'_+ + E'_- \quad (65)
$$

where

$$
E'_+ = \frac{1}{2}(E'+\lambda U) \quad (66)
$$
$$
E'_- = \frac{1}{2}(E'-\lambda U) \quad (67)
$$
$$
(68)
$$

where λ is chosen to be larger than the local maximum eigenvalues of E':

$$
\lambda = \frac{|\nabla\xi|}{J}\left(\sqrt{(\epsilon c)^2+u'^2}+c\right) \quad (69)
$$

where

$$
u' = \frac{\xi_x u+\xi_y v+\xi_z w+\xi_t}{|\nabla\xi|} \quad (70)
$$

The parameter ϵ is a small positive constant added for the smoothness of the splitting. The flux E'_+ and E'_- contain only positive and negative eigenvalues respectively. Therefore, in the spatial discretization of Eq. (10), the flux derivatives are split into two terms

$$\frac{\partial E'}{\partial \xi} = \frac{\partial E'_+}{\partial \xi} + \frac{\partial E'_-}{\partial \xi} \tag{71}$$

where the first term on the right hand side is discretized by an upwind high-order finite-difference method and the second term is discretized by a downwind high-order finite-difference method.

Numerical diffusion is introduced in the Lax-Friedrichs schemes by the splitting of the flux vector. The first-order upwind schemes using the Lax-Friedrichs schemes is very numerically diffusive. On the other hand, the inviscid fluxes can also be split according to their characteristic fields [46], which is less diffusive. But the characteristic splitting is computationally more expansive and the numerical diffusions of the Lax-Friedrichs schemes become much smaller when fourth or higher order upwind schemes are used for the flow field without shock waves.

Discretization of Transport Flux Vectors

For the compressible Navier-Stokes equations (10) in a conservation-law form, the second-order derivatives do not appear explicitly in the equations. Instead, they appear as first-order derivatives in the transport flux vectors in Eq. (4). For such equations, it is easier to discretize the transport terms by applying central finite-difference operators for the first derivative twice [47]. The approximation of the first-order derivative for computing the viscous terms can be done using standard central compact or explicit schemes with one-sided difference approximation For example, the sixth-order central inner schemes (5-3-3-1) and the sixth-order compact boundary schemes are as follows:

$$60u'_0 + 300u'_1 = \frac{1}{h}(-197u_0 - 25u_1 + 300u_2 - 100u_3 + 25u_4 - 3u_5) \tag{72}$$

$$\frac{15}{2}u'_0 + 60u'_1 + 45u'_2 = \frac{1}{h}\left(-\frac{215}{8}u_0 - 50u_1 + \frac{135}{2}u_2 + 10u_3 - \frac{5}{8}u_4\right) \tag{73}$$

$$b_{i-1}\,u'_{i-1} + b_i\,u'_i + b_{i+1}\,u'_{i+1} = \frac{1}{h}\sum_{k=-2}^{2} a_{i+k}\,u_{i+k} \quad (i = 2, 3, \cdots, N-2) \tag{74}$$

$$45u'_{N-2} + 60u'_{N-1} + \frac{15}{2}u'_N = \frac{1}{h}\left(\frac{215}{8}u_N + 50u_{N-1} - \frac{135}{2}u_{N-2} - 10u_{N-3} + \frac{5}{8}u_{N-4}\right) \tag{75}$$

$$60u'_N + 300u'_{N-2} = \frac{1}{h}(197u_N + 25u_{N-1} - 300u_{N-2} + 100u_{N-3} - 25u_{N-4} + 3u_{N-5}) \tag{76}$$

where the coefficients for the inner schemes are given by Eq. (57) with $\alpha = 0$. The formulas can be written into matrix form

$$\mathbf{B}U' = \mathbf{A}U \tag{77}$$

where $U = (u_0, \cdots, u_N)^T$. The derivative of the viscous flux in Eq. (10) can be discretized using the same first-order operator above. The second-order approximation is 6th-order accurate even though the order at the boundary may be degenerated. Though such discretization leads to a wider grid stencil than using central compact schemes to second-order derivative directly, the eigenvalue analysis shows that such an approach using the sixth-order central schemes with boundary closures is stable when it is applied to the one-dimensional linear heat equation. Other similar central compact and explicit high-order schemes for second-order derivatives can be obtained easily.

Semi-Implicit Runge-Kutta Schemes for Temporal Discretization

The spatial discretization of the governing equations leads to a system of first-order ordinary differential equations for the flow variables, and the accelerations and speeds of the shock fronts. For reacting hypersonic flow simulations, the thermo-chemical source term W is often stiff in temporal discretization. In Ref. [42,43], Zhong derived three kinds of high-order semi-implicit Runge-Kutta schemes for high-order temporal integration of the governing equations. These schemes additively split the governing equations into stiff and non-stiff terms in the form of

$$\frac{d\mathbf{u}}{dt} = \mathbf{f}(\mathbf{u}) + \mathbf{g}(\mathbf{u}) \tag{78}$$

where $\mathbf{u}$ is the vector of discretized flow field variables, $\mathbf{f}$ is non-stiff terms resulted from spatial discretization of the flux terms which can be computed explicitly, and $\mathbf{g}$ is stiff thermo-chemical source terms which need to be computed implicitly. The coefficients of the semi-implicit schemes were derived such that they are high-order accurate with the simultaneous coupling between the implicit and explicit terms. In addition, the schemes are unconditionally stable for the stiff terms when a CFL condition is satisfied for the explicit terms.

Three versions of 3-stage third-order semi-implicit Runge-Kutta schemes have been derived to integrate Eq. (78) by simultaneously treating $\mathbf{f}$ explicitly and $\mathbf{g}$ implicitly. The three versions of the third-order accurate ASIRK time-stepping methods are:

ASIRK-3A Method:

$$\begin{cases} \mathbf{k}_1 &= h\{\mathbf{f}(\mathbf{u}^n) + \mathbf{g}(\mathbf{u}^n + a_1\mathbf{k}_1)\} \\ \mathbf{k}_2 &= h\{\mathbf{f}(\mathbf{u}^n + b_{21}\mathbf{k}_1) \\ & \quad +\mathbf{g}(\mathbf{u}^n + c_{21}\mathbf{k}_1 + a_2\mathbf{k}_2)\} \\ \mathbf{k}_3 &= h\{\mathbf{f}(\mathbf{u}^n + b_{31}\mathbf{k}_1 + b_{32}\mathbf{k}_2) \\ & \quad +\mathbf{g}(\mathbf{u}^n + c_{31}\mathbf{k}_1 + c_{31}\mathbf{k}_2 + a_3\mathbf{k}_3)\} \\ \mathbf{u}^{n+1} &= \mathbf{u}^n + \omega_1\mathbf{k}_1 + \omega_2\mathbf{k}_2 + \omega_3\mathbf{k}_3 \end{cases}$$

ASIRK-3B Method:

$$\begin{cases} [\mathbf{I} - ha_1\mathbf{J}(\mathbf{u}^n)]\,\mathbf{k}_1 = h\{\mathbf{f}(\mathbf{u}^n) + \mathbf{g}(\mathbf{u}^n)\} \\ [\mathbf{I} - ha_2\mathbf{J}(\mathbf{u}^n)]\,\mathbf{k}_2 = \\ \qquad h\{\mathbf{f}(\mathbf{u}^n + b_{21}\mathbf{k}_1) \\ \qquad + \mathbf{g}(\mathbf{u}^n + c_{21}\mathbf{k}_1)\} \\ [\mathbf{I} - ha_3\mathbf{J}(\mathbf{u}^n)]\,\mathbf{k}_3 = \\ \qquad h\{\mathbf{f}(\mathbf{u}^n + b_{31}\mathbf{k}_1 + b_{32}\mathbf{k}_2) \\ \qquad + \mathbf{g}(\mathbf{u}^n + c_{31}\mathbf{k}_1 + c_{32}\mathbf{k}_2)\} \\ \mathbf{u}^{n+1} = \mathbf{u}^n + \omega_1\mathbf{k}_1 + \omega_2\mathbf{k}_2 + \omega_3\mathbf{k}_3 \end{cases}$$

ASIRK-3C Method:

$$\begin{cases} [\mathbf{I} - ha_1\mathbf{J}(\mathbf{u}^n)]\,\mathbf{k}_1 = h\{\mathbf{f}(\mathbf{u}^n) + \mathbf{g}(\mathbf{u}^n)\} \\ [\mathbf{I} - ha_2\mathbf{J}(\mathbf{u}^n + c_{21}\mathbf{k}_1)]\,\mathbf{k}_2 = \\ \qquad h\{\mathbf{f}(\mathbf{u}^n + b_{21}\mathbf{k}_1) + \\ \qquad \mathbf{g}(\mathbf{u}^n + c_{21}\mathbf{k}_1)\} \\ [\mathbf{I} - ha_3\mathbf{J}(\mathbf{u}^n + c_{31}\mathbf{k}_1 + c_{32}\mathbf{k}_2)]\,\mathbf{k}_3 = \\ \qquad h\{\mathbf{f}(\mathbf{u}^n + b_{31}\mathbf{k}_1 + b_{32}\mathbf{k}_2) + \\ \qquad \mathbf{g}(\mathbf{u}^n + c_{31}\mathbf{k}_1 + c_{32}\mathbf{k}_2)\} \\ \mathbf{u}^{n+1} = \mathbf{u}^n + \omega_1\mathbf{k}_1 + \omega_2\mathbf{k}_2 + \omega_3\mathbf{k}_3 \end{cases}$$

The first method uses diagonally implicit Runge-Kutta methods for stiff term $\mathbf{g}$, which leads to a nonlinear equation at every stage of the implicit calculations if $\mathbf{g}$ is a nonlinear function of $\mathbf{u}$. The second and third methods use linearized implicit schemes for the stiff term $\mathbf{g}$. Methods B and C, which are similar to linearized implicit methods commonly used in computing reactive flows [48], are more efficient than the full implicit method A. However, for some stiff nonlinear problems, method A is necessary because it is more stable than the Rosenbrock semi-implicit Runge-Kutta method. These third-order Semi-Implicit Runge-Kutta methods are used for time-accurate computations in the direct simulation of transient hypersonic boundary layers.

The parameters of the semi-implicit Runge-Kutta methods were chosen based on both stability and accuracy requirements with the simultaneous coupling between the explicit and implicit terms. The optimal parameters were computationally searched by simultaneously imposing the stability and accuracy conditions discussed above. The coefficients obtained and analyzed in Ref. [43] are

ASIRK-3A, ASIRK-3B, and ASIRK-3C:

$\omega_1 = \frac{1}{8}$	$\omega_2 = \frac{1}{8}$	$\omega_3 = \frac{3}{4}$
$b_{21} = \frac{8}{7}$	$b_{31} = \frac{71}{252}$	$b_{32} = \frac{7}{36}$

ASIRK-3A:

$a_1 = .485561$	$a_2 = .951130$	$a_3 = .189208$
$c_{21} = .306727$	$c_{31} = .45$	$c_{32} = -.263111$

ASIRK-3B:

$a_1 = 1.40316$	$a_2 = .322295$	$a_3 = .315342$
$c_{21} = 1.56056$	$c_{31} = \frac{1}{2}$	$c_{32} = -.696345$

ASIRK-3C:

$a_1 = .797097$	$a_2 = .591381$	$a_3 = .134705$
$c_{21} = 1.05893$	$c_{31} = \frac{1}{2}$	$c_{32} = -.375939$

where a_1, a_2, a_3, c_{21}, and c_{32} are irrational numbers with six significant digits. The double-precision values of these parameters can be found in Ref. [43].

Numerical Results

A three-dimensional solver has been written by using explicit high-order upwind schemes for the spatial discretization with a high-order shock fitting algorithm. The compact schemes will be implemented later. The spatial discretization has the option of a third-order upwind scheme [31], fifth-order upwind (60), and seventh-order upwind schemes (64). In the shock fitting algorithm, the derivatives of the shock shape H_ξ, H_ζ, $H_{\tau\xi}$, and $H_{\tau\zeta}$ are needed in the shock fitting algorithm. They are numerically evaluated using the standard sixth-order compact central scheme shown in Eqs. (72) to (76).

1. Linear Wave Equation (1-D)

The compact and explicit upwind schemes presented in this paper are tested with numerical computations of the 1-D linear wave equations given in Eq. (52). The parameters of the calculations are: $a = 0$, $b = 1$, $c = 1$, $N + 1$ uniform grid points, and the initial condition is

$$u(x,0) = \sin(\omega\pi x) \qquad 0 \le x \le 1 \qquad (79)$$

Both periodic and non-periodic boundary conditions are used to test the accuracy of schemes with and without boundary closures. In order to compare the spatial accuracy of the schemes, the time marching scheme is a third-order Runge-Kutta scheme using a very small time step corresponding to a CFL number of 0.005. The grid refinement in time is used to ensure that the solutions are independent of the temporal step sizes so that the temporal errors are much smaller than the spatial errors.

The sixth-order standard central compact scheme with stable 3,4-6-4,3 boundary closure and a fourth-order compact central 7-3-5-2 scheme of Lele [32] for spectral-like resolution are also tested. The 7-3-5-2 optimized scheme is fourth-order accurate but has smaller phase errors at large ω. Though the order of the scheme is lower than the maximum achievable order for a given stencil, the degree of freedom in deriving the coefficients is used to minimize the phase errors in resolving high wave-number modes. Compared with schemes with maximum order accuracy, the optimized schemes have lower accuracy for resolving modes of small ω, but they have higher accuracy in resolving modes of larger ω. It is expected that the optimized schemes resolve a range of length scales better than the maximum order schemes. Similar approaches have also been used in optimizing finite difference schemes for various applications [40,41,49,50].

The formal orders of accuracy of the new schemes are tested by computing the wave equation with a fixed $\omega = 2$ and three sets of grids: $N = 25, 50, 100$. For a global p-th order scheme, the error should be reduced by a factor of 2^p times when grid size is reduced by half. The results are shown in Table 2. The results in the table confirm the formal orders of accuracy of the schemes. The numerical stability also agrees with the eigenvalue analysis. The results also show that the accuracy of the boundary closure dominates the overall accuracy of the schemes. For the 3,4-6-4,3 central compact scheme, the result is less accurate than the upwind 4,4-5-4,4 schemes because the central scheme is only third-order accurate. The table also shows that the accuracy of the upwind compact 7-3-3-1 schemes is substantially low when fifth-order compact boundary schemes are used. But the fifth-order accuracy of the 7-3-3-1 schemes is obtained when they are coupled with fifth-order explicit boundary schemes. The reason seems to be that the compact boundary closures are more unstable than the explicit boundary schemes. More studies are needed to resolve this issue.

2. Supersonic Couette Flow Stability (2-D)

Compressible Couette flow is a wall-bounded parallel shear flow which is a simple example of hypersonic shear flows. In Ref. [51], we have developed two computer codes using a fourth-order finite-difference global method and a spectral global method to compute the linear stability of the supersonic Couette flow, as well as boundary layer flows. The accuracy of the LST analysis is checked by comparing the results obtained from the two approaches.

Because the mean flow is a parallel flow, the linear stability analysis based on the full Navier-Stokes equations does not involve the parallel approximation of a developing boundary layer. Therefore, we use the compressible two-dimensional Couette flow to test the numerical accuracy of the new high-order upwind schemes for solving the time-accurate Navier-Stokes equations. The shock fitting procedure is turned off because there is no shock. Both steady and unsteady two-dimensional computations are tested.

a. Steady Flow Solutions

We first used the 5th-order explicit upwind Navier-Stokes code to compute the steady solutions of the supersonic Couette flow. The results are compared with "exact" solutions obtained by a shooting method with several order of magnitudes smaller errors. The flow variables are nondimensionlized by their corresponding values at the upper wall. The numerical simulation are conducted using several sets of uniform grids in order

Table 1: Numerical errors for computations of supersonic Couette flow using high-order upwind schemes. ($e_1 = ||e||_1$ and $e_2 = ||e||_2$)

Third Order Scheme					
Grids	α	$e_1 \times 10^{-7}$	ratio	$e_2 \times 10^{-7}$	ratio
31	0.125	64.0	–	12.9	–
61	0.125	7.25	8.8	0.991	13
Fifth Order Scheme					
Grids	α	$e_1 \times 10^{-7}$	ratio	$e_2 \times 10^{-7}$	ratio
31	−1	6.45	–	1.68	–
61	−1	0.238	27	0.0417	40

to evaluate the accuracy of the algorithm. Many test cases with different Mach number and wall temperature have been tested. The results shown in this paper are those for the following flow conditions: $M_\infty = 2$, the upper wall is an isothermal wall with dimensionless $T_\infty = 1$ while the lower wall is an adiabatic wall. The gas is assumed to perfect gas with $\gamma = 1.4$ and $Pr = 0.72$. The viscosity coefficient is calculated using the Sutherland's law,

$$\mu = T^{3/2}\left(\frac{1+C}{T+C}\right) \tag{80}$$

where C is a taken to be 0.5.

Figure 3 shows the steady temperature profile obtained by using a fifth-order upwind scheme with 121 uniform grid points. The numerical results agree well with the exact solutions. Figure 4 shows the same steady temperature profile. The numerical solutions are obtained using three sets of grids. The results show that all three sets of grids resolve the steady flow field very well. The quantitative numerical errors of the simulations using the three grids are listed in Table 1. The table shows that the numerical errors for a fifth order upwind scheme are of the order of 10^{-6} using 31 grid points and 0.4×10^{-7} using 61 grid points. The theoretical ratio of the errors between the coarse and the fine grids are 8 for a third-order scheme and 32 for a fifth-order scheme. The results in the table show that the numerical algorithms are able to maintain such high orders of accuracy.

b. Unsteady Flow Solutions

We conduct numerical simulations for the temporal stability of the compressible Couette flow by simulating the development of given initial disturbances in the two dimensional flowfield. The initial conditions are the steady flow solutions plus disturbances given by a set of eigenfunctions obtained by linear stability analysis. For small initial disturbances, the growth or decay of the disturbances are given by the eigenvalue of the eigen-mode.

The subsequent unsteady flow field is solved by computing the unsteady Navier-Stokes equations using the fifth-order upwind scheme. The same stretched grids are used in y direction as that used in the LST calculation [51]. The computational domain in the simulation is one period in length in the x direction. Periodic boundary conditions are used in the x direction. The flow conditions are: $M_\infty = 2$ and $Re_\infty = 1000$. For this case, the initial disturbance wave has a dimensionless wave number of $\alpha = 3$, and the eigenvalue obtained from the temporal linear stability analysis is

$$\begin{aligned} \omega &= \omega_r + \omega i \\ &= 5.52034015848 - 0.132786378788i \end{aligned} \tag{81}$$

where a negative ωi means that the disturbances will decay in time with a dimensionless frequency of ω_r.

Figure 5 shows the comparison of the DNS results and the LST prediction for the time history of pressure and temperature perturbations at a fixed point in the 2-D supersonic Couette flow field. The computation uses a 40×100 grid. The corresponding time history for velocity components is shown in Fig. 6. These figures show that the instantaneous perturbations of all flow variables for the 2-D numerical simulations agree very well with the linear stability analysis.

Figures 7 and 8 show the distribution of instantaneous flow perturbations in the x and y direction at the end of about six periods in time. Again the results agree well between the DNS results and the LST results.

The results of the two-dimensional simulation of the steady and unsteady flows for Couette flow stability show that the current fifth-order upwind scheme is high-order accurate and is suitable for stability and transition simulations.

3. Steady Hypersonic Flow Over a Cylinder

A test case of steady 2-D hypersonic flow over a cylinder is considered because there are experimental results and accurate numerical solutions obtained by a shock-fitting spectral method [52] available for comparison. The flow conditions are

$M_\infty = 5.73$

$Re_\infty = 2050$
$T_\infty = 39.6698K$
$T_w = 210.02K$
$\gamma = 1.4$
$Pr = 0.77$
Cylinder Radius: $r = 0.0061468m$

The numerical results are obtained by using the new fifth-order shock fitting schemes. Figure 9 shows a set of 80 × 60 grids used in the simulations for the shock fitting calculations. The grids are stretched in both the streamwise and the wall-normal direction. Figure 10 compares the computed temperature contours for flow over a circular cylinder. The upper half contours are the results obtained by the spectral method, taken from [52], and the lower half contours are current results using a 80 × 60 grid. The two solutions agree very well for all the points in the flow field.

The pressure coefficients along cylinder surface computed by the high-order finite difference shock fitting methods are compared with experimental results and spectral results [52] in Fig. 11. The heat transfer rates along the surface are compared in Fig. 12. The solutions of the Navier-Stokes equations obtained by the current fifth-order upwind scheme agree well with the spectral methods results. The slight differences between the numerical results and the experiments, which are consistent with other numerical results, may be due to the differences in flow conditions between the experiments and the simulation.

The grid convergence of the results are tested by refining the grids used for the simulation. Figures 13 and 14 compare the the surface pressure coefficients and heating rates along the surface for three sets of grids. The results show that the results are highly accurate for relatively coarse grids.

4. Receptivity of A Hypersonic Boundary Layer

The last test case considered is the numerical simulation of the receptivity of a two-dimensional boundary layer to weak freestream acoustic disturbance waves for hypersonic flow past a parabolic leading edge at zero angle of attack. The flow phenomena and the detailed descriptions of such flows are given in Ref. [53]. The purpose of the test case is to evaluate the numerical accuracy of such simulations for given grid points by grid refinement studies. We test the accuracy of the steady and unsteady computations using the fifth-order explicit upwind shock fitting methods using a set of 160 × 120 grids.

In the simulation, the freestream disturbances are superimposed on the steady mean flow to investigate the development of T-S waves in the boundary layer with the effects of the bow shock interaction. The freestream disturbances are assumed to be weak monochromatic planar acoustic waves with wave front normal to the center line of the body. The perturbations of flow variable introduced by the freestream acoustic wave before reaching the bow shock can be written in the following form:

$$\begin{Bmatrix} u' \\ v' \\ p' \\ \rho' \end{Bmatrix}_\infty = \begin{Bmatrix} |u'| \\ |v'| \\ |p'| \\ |\rho'| \end{Bmatrix}_\infty e^{ik[x-(1+M_\infty^{-1})t]} \quad (82)$$

where $|u'|$, $|u'|$, $|p'|$, and $|\rho'|$ are perturbation amplitudes satisfying the following relations:

$$|u'|_\infty = \epsilon\,, \qquad |v'|_\infty = 0$$
$$|p'|_\infty = \gamma M_\infty \epsilon\,, \qquad |\rho'|_\infty = M_\infty \epsilon$$

where ϵ is a small number representing the freestream wave magnitude. The parameter k is the dimensionless freestream wave number which is related to the dimensionless circular frequency ω by:

$$\omega = k\,(1 + M_\infty^{-1}) \quad (83)$$

The corresponding dimensionless frequency F is defined as

$$F = \frac{\omega^* \nu^*}{U_\infty^{*2}} = \omega / Re_\infty\,. \quad (84)$$

The body surface is a parabola given by

$$x^* = b^* y^{*2} - d^* \quad (85)$$

where b^* a given constant and d^* is taken as the reference length. The body surface is assumed to be a non-slip wall with an isothermal wall temperature T_w^*.

The specific flow conditions are:

$M_\infty = 5$ | $\epsilon = 1.5 \times 10^{-3}$
$T_\infty^* = 3434.62.989\,K$ | $p_\infty^* = 698.26\,Pa$
$T_w^* = 1000\,K$ | $\gamma = 1.4$
$R^* = 286.94\,Nm/kgK$ | $Pr = 0.72$
$b^* = 40\,m^{-1}$ | $d^* = 0.1\,m$
$T_r^* = 288\,K$ | $T_s^* = 110.33\,K$
$\mu^* = 0.17894 \times 10^{-4} kg/ms$
Nose Radius of Curvature $= r^* = 0.0125\,m$
$Re_\infty = \rho_\infty^* U_\infty^* d^* / \mu_\infty^* = 5025.12$

b. Steady Flow Solutions

The steady flow solutions of the Navier-Stokes equations for the viscous hypersonic flow over the parabola are obtained by using the new fifth-order explicit unsteady computer code and advancing the solutions to a steady state without freestream perturbations. Figure 15 shows steady flow solutions for a set of 160×120 computational grid, pressure contours, and Mach number contours.

The numerical resolution of the 160×120 grid is evaluated by comparing their solutions with fine 320×240 grid solutions. Figure 16 compares the steady solution of the bow shock shape in x-y coordinates for two set of grids. Figures 17 and 18 compare the pressure profile behind the bow shock shape and the pressure on the body surface for the two set of grids. Figure 19 shows the comparison for Mach number along the stagnation line. All these steady solutions show that the two sets of results agree with each other very well, and the steady solutions are well resolved by the grids.

b. Unsteady Flow Solutions

In this section, the generation of boundary-layer T-S and inviscid instability waves by freestream acoustic disturbances is considered for hypersonic flow over a parabolic leading edge with various freestream disturbance wave numbers or frequencies. The dimensionless freestream wave numbers are $k = 20$, and the corresponding dimensionless frequency $F \times 10^{-6}$ is 4776. Figure 20 shows the contours for the instantaneous temperature, pressure, and the velocity component in y direction in the unsteady simulation. The numerical solutions are obtained by using the 160×120 grids. The instantaneous contours show the development of first-mode instability waves in the boundary layer on the surface.

Again, grid refinement is used to check the numerical resolution of the 160×120 grids for unsteady DNS simulations by comparing with the results of the double grid case. The instantaneous solutions of the two test runs are compared on the body surface and behind the bow shock.

Figure 21 compares the distribution of instantaneous entropy perturbations along the parabola surface. The distribution of instantaneous entropy perturbations along the bow shock surface is plotted in Fig. 22. The unsteady solutions of the two sets of grids agree very well. Therefore the current grids for the new fifth-order upwind schemes resolve the instability wave well. Figure 23 shows the numerical results of the instantaneous normal bow shock velocities vs. the shock x coordinates for the case of $k = 15$. Again the grid resolution for the instability waves is satisfactory.

In the unsteady simulations, the bow shock oscillates due to freestream disturbances and the reflection of acoustic waves from the boundary layer to the shock. It is important that the numerical simulation resolves the unsteady shock motion accurately. The current high-order shock fitting method is found to be able to compute the unsteady flow fields and the unsteady shock motion very accurately. A simple way to check the accuracy of the numerically computed unsteady shock/disturbances interaction is shown in Fig. 24, which shows the time history of the instantaneous pressure perturbation at the point immediately behind the bow shock at the center line for the case of $k = 40$. In the initial moment of imposing the freestream disturbances, there is no reflected waves from the undisturbed steady boundary layer. The freestream disturbance wave transmission relation can be predicted by linear theory such as that derived by Mckenzie and Westphal [54]. At later time, the wave pattern changes because the disturbance waves enter the boundary layer and generate reflected waves back to the shock. The figure shows very good agreement between DNS and linear predictions on the pressure perturbation due to freestream disturbances.

Figure 25 compares the time history of the instantaneous pressure perturbation at the point immediately behind the bow shock at the center line for the two grids. The results agree very well for the two cases.

Again, these results show that the current unsteady simulations with fifth-order accurate shock fitting are highly accurate for hypersonic boundary layer DNS studies.

Conclusions

This paper has presented and tested a new high-order upwind finite difference shock fitting method for the direct numerical simulations of hypersonic flows with strong bow shocks. The results of accuracy tests of the new fifth-order shock-fitting method are presented in this paper for four test cases: 1-D wave equation, 2-D DNS of stability of supersonic Couette flow, steady viscous hypersonic flow over a circular cylinder, and finally, the DNS of receptivity to freestream acoustic disturbances for hypersonic boundary layer over a parabola. The results show that the new schemes are very accurate for steady and unsteady simulations of hypersonic flows with a bow shock. Work is currently underway to extend the methods for DNS of hypersonic

flows over three-dimensional non-axisymmetric blunt cones.

Acknowledgments

This research was supported by the Air Force Office of Scientific Research under grant numbers F49620-94-1-0019 and F49620-95-1-0405 monitored by Dr. Len Sakell.

References

[1] National Research Council (U.S.). Committee on Hypersonic Technology for Military Application. Hypersonic Technology for Military Application. *Technical Report*, National Academy Press, Washington, DC., 1989.

[2] Defense Science Board. Final Report of the Second Defense Science Board Task Force on the National Aero-Space Plane (NASP). *AD-A274530, 94-00052, November*, 1992.

[3] L. Kleiser and T. A. Zang. Numerical Simulation of Transition in Wall-Bounded Shear Flows. *Ann. Rev. Fluid Mech.*, Vol. 23, pp. 495–535, 1991.

[4] H. L. Reed. Direct Numerical Simulation of Transition: the Spatial Approach. *Progress in Transition Modeling*, AGARD-Report-793 1994.

[5] L. Klerser and E. Laurien. Numerical Investigation of Interactive Transition Control. *AIAA Paper 85-0566*, 1985.

[6] Thomas A. Zang and M. Y. Hussaini. Numerical experiments on subcritical transition mechanisms. *AIAA Paper 81-1227*, 1981.

[7] H. Fasel. Investigation of the Stability of Boundary Layers by a Finite Difference Model of the Navier-Stokes Equations. *Journal of Fluid Mechanics*, Vol. 78, pp. 355–383, 1976.

[8] U. Rist and H. Fasel. Direct Numerical Simulation of Controlled Transition in Flat-Plate Boundary Layer. *Journal of Fluid Mechanics*, Vol. 298, pp. 211–248, 1995.

[9] M. M. Rai and P. Moin. Direct Numerical Simulation of Transition and Turbulence in a Spatially Evolving Boundary Layer. *Journal of Computational Physics*, Vol. 109, pp. 169–192, 1993.

[10] G. Danabasoglu, S. Biringen, and C. L. Strett. Spatial Simulation of Boundary Layer Instability: Effects of Surface Roughness. *AIAA Paper 93-0075*, 1993.

[11] C. Liu and Z. Liu. Multigrid Methods and High Order Finite Difference for Flow in Transition. *AIAA Paper 93-3354*, July, 1993.

[12] H. Bestek, M. Kloker, and W. Muller. Spatial Direct Numerical Simulation of Boundary Layer Transition Under Adverse Pressure Gradient. *Application of Direct and Large Eddy Simulation to Transition and Turbulence*, AGARD-CP-551, 1994.

[13] R. D. Joslin, C. L. Strett, and C.-L. Chang. Spatial Direct Numerical Simulation of Boundary-Layer Transition Mechanisms: Validation of PSE Theory. *Theoretical and Computational Fluid Dynamics*, Vol. 4, pp. 271–288, 1993.

[14] R. D. Joslin. Direct Numerical Simulation of Evolution and Control of 3-D Instability in Attachment-Line Boundary Layers. *Journal of Fluid Mechanics*, Vol. 291, pp. 369–392, 1995.

[15] G. Erlebacher and M. Y. Hussaini. Numerical experiments in supersonic boundary-layer stability. *Physics of Fluids: A*, 2:94–104, 1990.

[16] L. L. Ng and G. Erlebacher. Secondary instability in compressible boundary layers. *Physics of Fluids: A*, 4:710–717, 1992.

[17] A. Thumm, W. Wolz, and H. Fasel. Numerical Simulation of Spatially Growing Three-Dimensional Disturbance Waves in Compressible Boundary Layers. *in Laminar-Turbulent Transition, IUTAM Symposium, Toulouse, France, 1989, D. Arnal, R. Michel, Editors*, Springer-Verlag Berlin, 1990.

[18] H. Fasel, A. Trumm, and H. Bestek. Direct numerical simulation of transition in supersonic boundary layer: Oblique breakdown. In *Transitional and Turbulent Compressible Flows, ASME FED-Vol. 151*, 1993.

[19] W. Eibler and H. Bestek. Spatial Numerical Simulations for Nonlinear Transition Phenomena in Supersonic Boundary Layers. *Transitional and Turbulent Compressible Flows*, L. D. Kral and T. A. Zang, editors, pp. 69-76, FED-Vol. 151, ASME, 1993.

[20] W. Eibler and H. Bestek. Spatial Numerical Simulations of Linear and Weakly Nonlinear Instabilities in Supersonic Boundary Layers. *Theoretical and Computational Fluid Dynamics*, Vol. 8, pp. 219-235, 1996.

[21] N. A. Adams and L. Kleiser. Numerical simulation of transition in a compressible flat plate boundary layer. In *Transitional and Turbulent Compressible Flows, ASME FED-Vol. 151*, 1993.

[22] N. A. Adams. Subharmonic Transition to Turbulence in a Flat-Plate Boundary Layer at Mach Number 4.5. *Journal of Fluid Mechanics*, Vol. 317, pp. 301–335, 1996.

[23] Y. Guo, N. A. Adams, N. D. Sandham, and L. Kleiser. Numerical Simulation of Supersonic Boundary Layer Transition. *Application of Direct and Large Eddy Simulation to Transition and Turbulence*, AGARD-CP-551, 1994.

[24] C. D. Pruett and T. A. Zang. Direct Numerical Simulation of Laminar Breakdown in High-Speed Axisymmetric Boundary Layers. *Theoretical and Computational Fluid Dynamics*, Vol. 3, pp. 345–367, 1992.

[25] C. D. Pruett and C. L. Chang. A Comparison of PSE and DNS for High-Speed Boundary-Layer Flows. *Transitional and Turbulent Compressible Flows*, L. D. Kral and T. A. Zang, editors, pp. 57-67, FED-Vol. 151, ASME, 1993.

[26] C. D. Pruett, T. A. Zang, C.-L. Chang, and M. H. Carpenter. Spatial Direct Numerical Simulation of High-Speed Boundary-Layer Flows, Part I: Algorithmic Considerations and Validation. *Theoretical and Computational Fluid Dynamics*, Vol. 7, pp. 49–76, 1995.

[27] C. D. Pruett. Spatial Direct Numerical Simulation of Transitioning High-Speed Flows. *Transitional and Turbulent Compressible Flows*, L. D. Kral, E. F. Spina, and C. Arakawa, editors, pp. 63-70, FED-Vol. 224, ASME, 1995.

[28] X. Zhong. Additive Semi-Implicit Runge-Kutta Schemes for Computing High-Speed Nonequilibrium Reactive Flows. *Journal of Computational Physics*, Vol. 128, pp. 19-31, 1996.

[29] M. Y. Hussaini, D. A. Kopriva, M. D. Salas, and T. A. Zang. Spectral Methods for the Euler Equations: Part II–Chebyshev Methods and Shock Fitting. *AIAA Journal*, Vol. 23, No. 1, pp. 234–240, 1985.

[30] W. Cai. High-Order Hybrid Numerical Simulations of Two-Dimensional Detonation Waves. *AIAA Journal*, Vol. 33, No. 7, pp. 1248–1255, 1995.

[31] X. Zhong. Upwind compact and explicit high-order finite difference schemes for direct numerical simulation of high-speed flows. *submitted to the Journal of Computational Physics*, April 1996.

[32] S. K. Lele. Compact Finite Difference Schemes with Spectral-like Resolution. *Journal of Computational Physics*, Vol. 103, pp. 16–42, 1992.

[33] C. A. Kennedy and M. H. Carpenter. Several New Numerical Methods for Compressible Shear-Layer Simulations. *Applied Numerical Mathematics*, Vol. 14, pp. 397–433, 1994.

[34] M. H. Carpenter, D. Gotlieb, and S. Abarbanel. The Stability of Numerical Boundary Treatments for Compact High-Order Finite-Difference Schemes. *Journal of Computational Physics*, Vol. 108, pp. 272–295, 1993.

[35] M. H. Carpenter, D. Gotlieb, and S. Abarbanel. Stable and Accurate Boundary Treatments for Compact, High-Order Finite-Difference Schemes. *Applied Numerical mathematics*, Vol. 12, pp. 55–87, 1983.

[36] B. Gustafsson. The Convergence Rate for Difference Approximations to Mixed Initial Boundary Value Problems. *Mathematics of Computation*, Vol. 29, No. 130, pp. 396–406, 1975.

[37] M. M. Rai and P. Moin. Direct Simulations of Turbulent Flow Using Finite Difference Schemes. *Journal of Computational Physics*, Vol. 96, pp. 15–53, 1991.

[38] A. I. Tolstykh. On a Class of Noncentered Compact Difference Schemes of Fifth Order, Based on Pade Approximants. *Soviet Math. Dokl.*, Vol. 44, No. 1, pp. 69–74, 1991.

[39] I. Christie. Upwind Compact Finite Difference Schemes. *Journal of Computational Physics*, Vol. 59, pp. 353–368, 1985.

[40] D. W. Zingg, H. Lomax, and H. Jurgens. High-Accuracy Finite-Difference Schemes for Linear Wave Propagation. *SIAM Journal of Scientific Comput.*, Vol. 17, No. 2, pp. 328–346, 1995.

[41] N. A. Adams and K. Shariff. A High-Resolution Hybrid Compact-ENO Scheme for Shock-Turbulence Interaction Problems. *Center for Turbulence Research, Stanford University, California*, Manuscript 155, March 1995.

[42] X. Zhong. New High-Order Semi-implicit Runge-Kutta Schemes for Computing Transient Nonequilibrium Hypersonic Flow. *AIAA Paper 95-2007*, 1995.

[43] X. Zhong. Semi-Implicit Runge-Kutta Schemes for Direct Numerical Simulation of Transient High-Speed Reactive Flows. *To appear in the Journal of Computational Physics*, 1996.

[44] J. D. Anderson. *Hypersonic and High Temperature Gas Dynamics.* McGraw-Hill, 1989.

[45] Y. Liu and M. Vinkur. Nonequilibrium Flow Computations. I. An Analysis of Numerical Formulations of Conservation Laws. *Journal of Computational Physics*, Vol. 83, pp. 373–397, 1989.

[46] C.-W. Shu and S. Osher. Efficient implementation of essentially non-oscillatory schemes II. *Journal of Computational Physics*, 83:32–78, 1989.

[47] B. Sjogreen. High Order Centered Difference Methods for the Compressible Navier-Stokes Equations. *Journal of Computational Physics*, Vol. 117, pp. 67–68, 1995.

[48] R. J. Leveque and H. C. Yee. A study of numerical methods for hyperbolic conservation laws with stiff source terms. *J. of Computational Physics*, 86:187–210, 1990.

[49] C. K. W. Tam and J. C. Webb. Dispersion-Relation-Preserving Finite Difference Schemes for Computational Acoustics. *Journal of Computational Physics*, Vol. 107, pp. 262–281, 1993.

[50] Z. Haras and S. Ta'asan. Finite Difference Schemes for Long-Time Integration. *Journal of Computational Physics*, Vol. 114, pp. 265–279, 1994.

[51] S. H. Hu and X. Zhong. Linear Stability of Compressible Couette Flow. *AIAA paper 97-0432*, 1997.

[52] D. A. Kopriva. Spectral Solution of the Viscous Blunt Body Problem. *AIAA Journal*, 31, 7, 1993.

[53] X. Zhong. Direct Numerical Simulation of Hypersonic Boundary-Layer Transition Over Blunt Leading Edges, Part II: Receptivity to Sound (Invited). *AIAA paper 97-0756, 35th AIAA Aerospace Sciences Meeting and Exhibit, January 6-9, Reno, Nevada*, 1997.

[54] J. F. Mckenzie and K. O. Westphal. Interaction of linear waves with oblique shock waves. *The Physics of Fluids*, 11(11):2350–2362, November 1968.

Table 2: L^1 **Errors of solving wave equation with non-periodic boundary conditions using schemes with numerical boundary closures. The initial condition is $u(x,0) = \sin(2\pi x)$. For each scheme, three sets of grids N are used in a fixed computational domain to compute the error ratios by grid refinement.**

Schemes		N	e_1	$e_1(N)/e_1(N/2)$
Inner:	3-1-3-1 (Upwind, $\alpha = .25$)	25	.519 (-3)	
BC:	3,3-3-3,3 explicit	50	.230 (-4)	.226 (+2)
Order:	3	100	.192 (-5)	.120 (+2)
Inner:	5-2-1-0 (Central, $\alpha = 0$)	25	.363 (-3)	
BC:	3,3-3-3,3 explicit	50	.727 (-4)	.500 (+1)
Order:	3	100	.453 (-5)	.160 (+2)
Inner:	5-2-1-0 (Upwind, $\alpha = .25$)	25	.520 (-3)	
BC:	3,3-3-3,3 explicit	50	.339 (-4)	.153 (+2)
Order:	3	100	.374 (-5)	.908 (+1)
Inner:	5-2-1-0 (Upwind-Bias Stencil, $\alpha = 2$)	25	.190 (-2)	
BC:	3,3-3-3,3 explicit	50	.273 (-3)	.697 (+1)
Order:	3	100	.375 (-4)	.728 (+1)
Inner:	7-3-3-1 (Central, $\alpha = 0$)	25	.972 (-3)	
BC:	3,4,4-6-4,4,3 compact	50	.350 (-4)	.277 (+2)
Order:	4	100	.246 (-5)	.142 (+2)
Inner:	7-3-5-2 (Central, Lele's Spectral-Like)	25	.646 (-4)	
BC:	4,4,4-4-4,4,4 compact	50	.103 (-4)	.629 (+1)
Order:	4	100	.327 (-6)	.314 (+2)
Inner:	5-2-3-1 (Central, $\alpha = 0$)	25	.635 (-4)	
BC:	4,4-5-4,4 compact	50	.560 (-5)	.113 (+2)
Order:	5	100	.163 (-6)	.343 (+2)
Inner:	5-2-3-1 (Upwind, $\alpha = -1$)	25	.112 (-3)	
BC:	4,4-5-4,4 compact	50	.351 (-5)	.319 (+2)
Order:	5	100	.110 (-6)	.319 (+2)
Inner:	7-3-1-0 (Upwind, $\alpha = -6$)	25	.124 (-3)	
BC:	4,4,4-5-4,4,4 explicit	50	.400 (-5)	.310 (+2)
Order:	5	100	.128 (-6)	.312 (+2)
Inner:	7-3-3-1 (Upwind, $\alpha = 36$)	25	.334 (-4)	
BC:	5,5,5-7-5,5,5 compact	50	.208 (-5)	.160 (+2)
Order:	6	100	.159 (-5)	.131 (+1)
Inner:	7-3-3-1 (Upwind, $\alpha = 36$)	25	.403 (-4)	
BC:	5,5,5-7-5,5,5 explicit	50	.636 (-6)	.633 (+2)
Order:	6	100	.996 (-8)	.639 (+2)
Inner:	9-4-1-0 (Upwind, $\alpha = 36$)	25	.472 (-4)	
BC:	5,5,5,5-7-5,5,5,5 explicit	50	.649 (-6)	.728 (+2)
Order:	6	100	.102 (-7)	.638 (+2)

Table 3: **Summary of upwind compact and explicit schemes with recommended values of α and the order of stable boundary closure schemes.**

Inner Scheme	Truncation	Stable B.C.	Recommended α
3-1-3-1	$\frac{\alpha}{4!}h^3u_i^{(4)}$	3-3-3	1/4
5-2-3-1	$\frac{\alpha}{6!}h^5u_i^{(6)}$	4,4-5-4,4 or 5,5-5-5,5	-1
7-3-3-1	$\frac{\alpha}{8!}h^7u_i^{(8)}$	5,5,5-7-5,5,5	36
5-2-1-0	$\frac{\alpha}{4!}h^3u_i^{(4)}$	3,3-3-3,3	1/4
7-3-1-0	$\frac{\alpha}{6!}h^5u_i^{(6)}$	4,4,4-5-4,4,4 or 5,5,5-5-5,5,5	-6
9-4-1-0	$\frac{\alpha}{8!}h^7u_i^{(8)}$	5,5,5,5-7-5,5,5,5	36

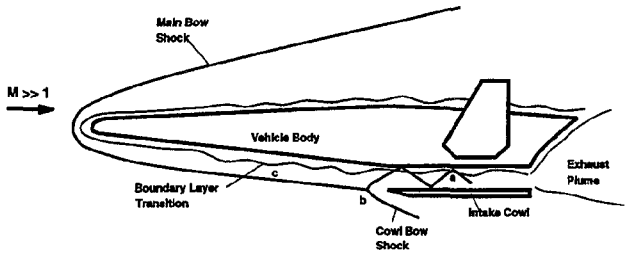

Figure 1: A schematic of a generic hypersonic lifting vehicle with boundary-layer transition.

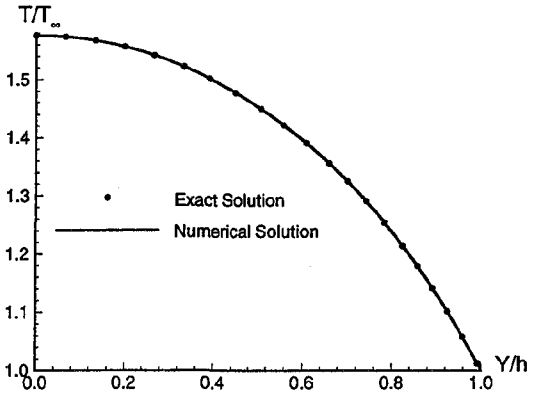

Figure 3: Variation of steady base flow temperature profile for adiabatic lower wall with $M_\infty = 2$. The numerical solution is obtained using a fifth-order upwind scheme using 121 grid points.

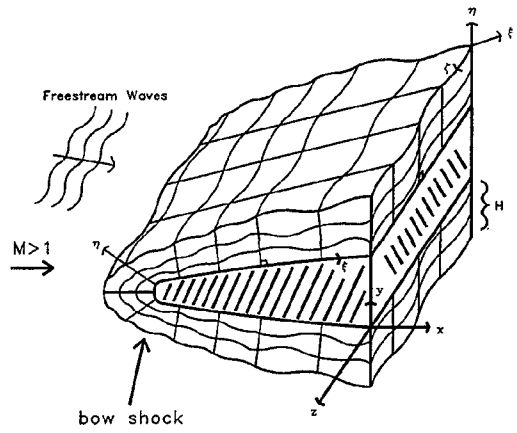

Figure 2: A schematic of 3-D shock fitted grids for the direct numerical simulation of hypersonic boundary-layer receptivity to freestream disturbances over a blunt leading edge.

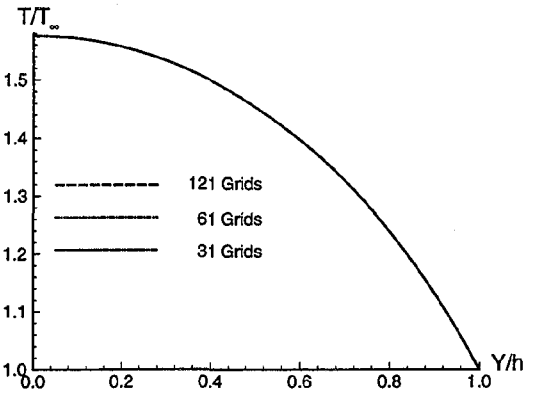

Figure 4: Variation of steady base flow temperature profile for adiabatic lower wall with $M_\infty = 2$. The numerical solutions are obtained using a fifth-order upwind scheme with three sets of grids.

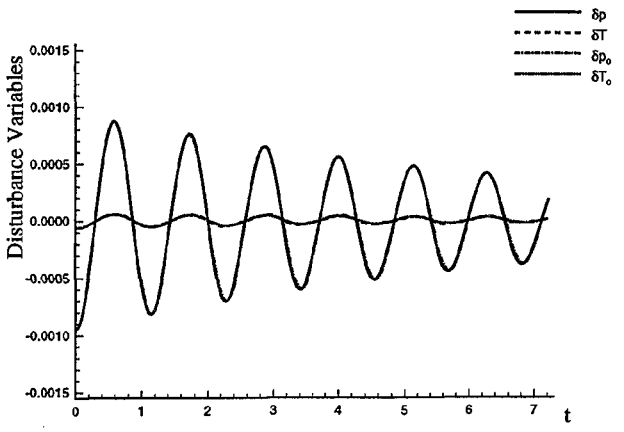

Figure 5: Time history of pressure and temperature perturbations at a fixed point in the 2-D supersonic Couette flow field. (LST: δp_0 and δT_0; DNS: δp and δT)

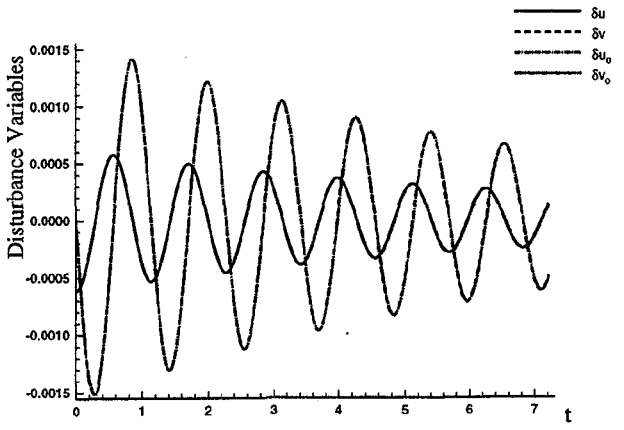

Figure 6: Time history of velocity component perturbations at a fixed point in the 2-D supersonic Couette flow field. (LST: δu_0 and δv_0; DNS: δu and δv)

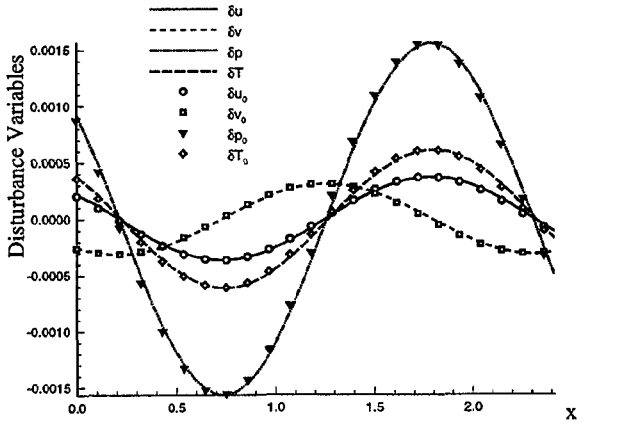

Figure 7: Distribution of instantaneous flow perturbations in x direction.

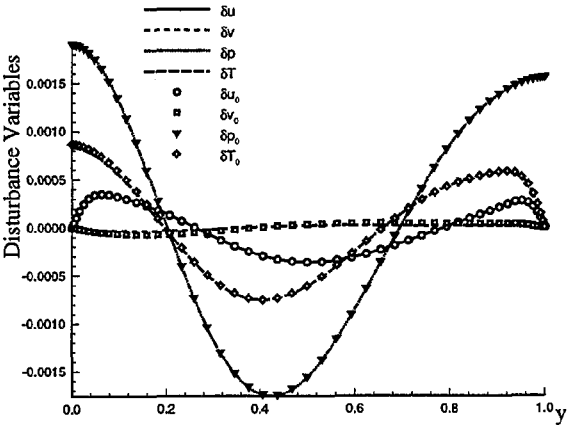

Figure 8: Distribution of instantaneous flow perturbations in y direction.

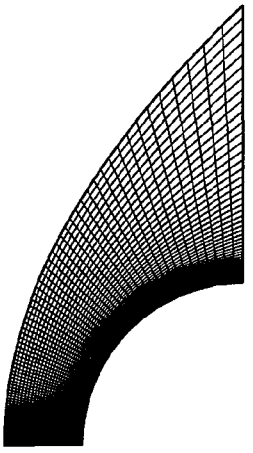

Figure 9: Computational grid for flow over a circular cylinder.

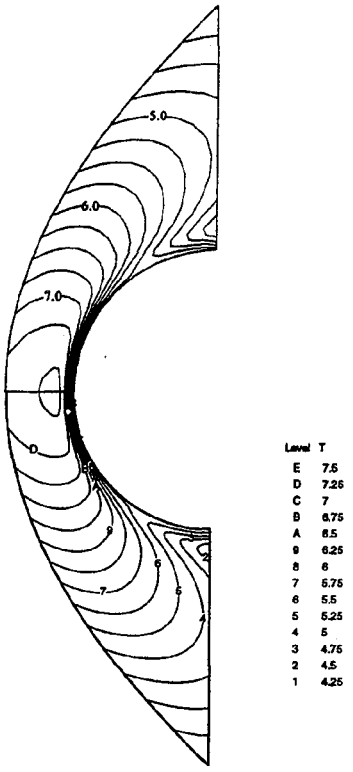

Figure 10: Comparison of computed temperature contours for flow over a circular. The upper half contours are taken from Kopriva (1993), and the lower half contours are current results using a 80×60 grid.

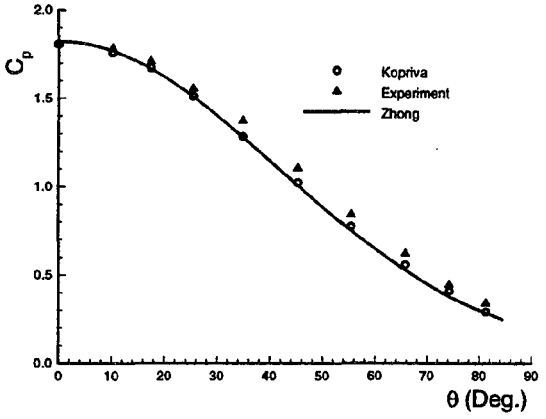

Figure 11: Comparison of pressure coefficients along cylinder surface.

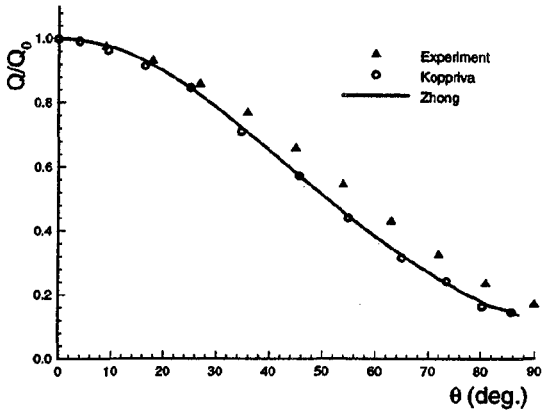

Figure 12: Comparison of heat transfer coefficients along cylinder surface.

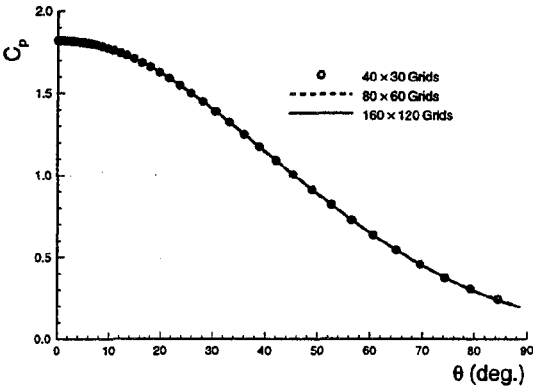

Figure 13: Comparison of pressure coefficients along cylinder surface. The results are obtained using three set of grids.

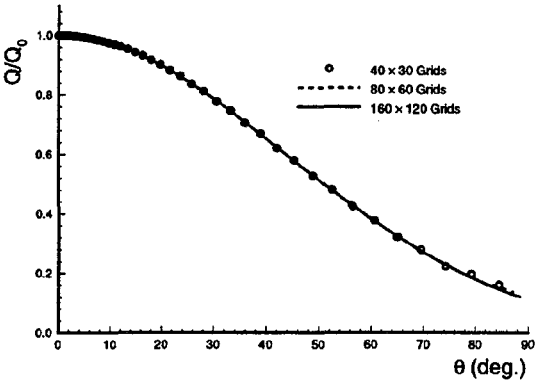

Figure 14: Comparison of heat transfer coefficients along cylinder surface. The results are obtained using three set of grids.

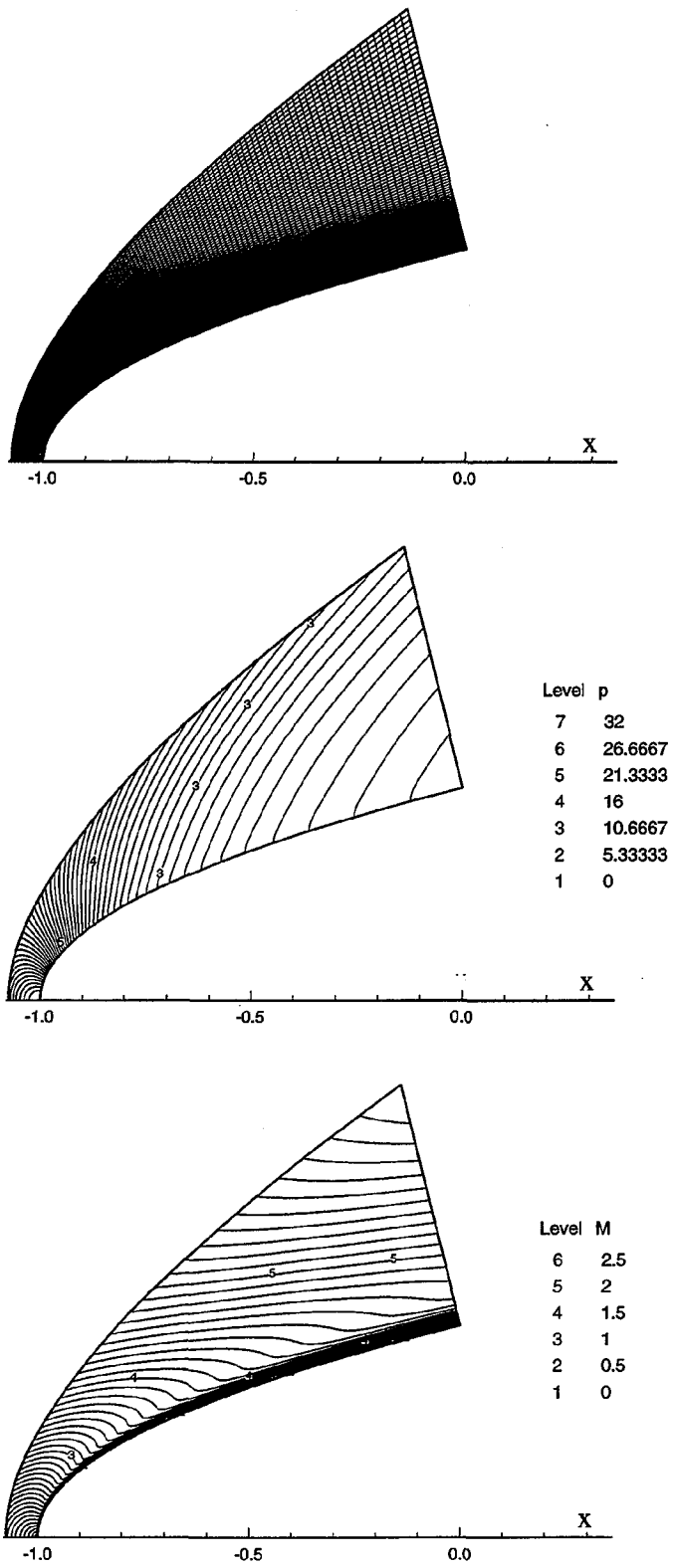

Figure 15: Steady flow solutions for computational grid (upper figure) where the bow shock shape is obtained as the freestream grid line, pressure contours (middle figure), and Mach number contours (lower figure).

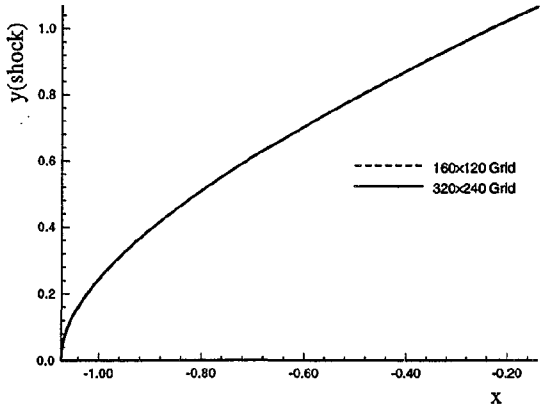

Figure 16: Comparison of steady solution of the bow shock shape in x-y coordinates for two set of grids.

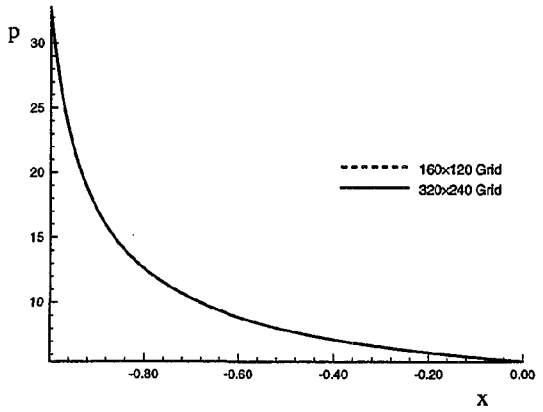

Figure 18: Comparison of steady solution of the pressure profile along the body surface for two set of grids.

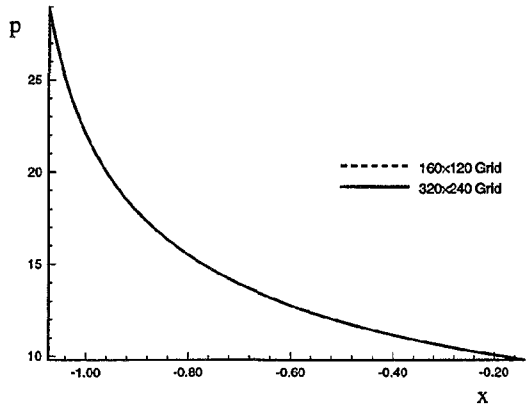

Figure 17: Comparison of steady solution of the pressure profile behind the bow shock shape for two set of grids.

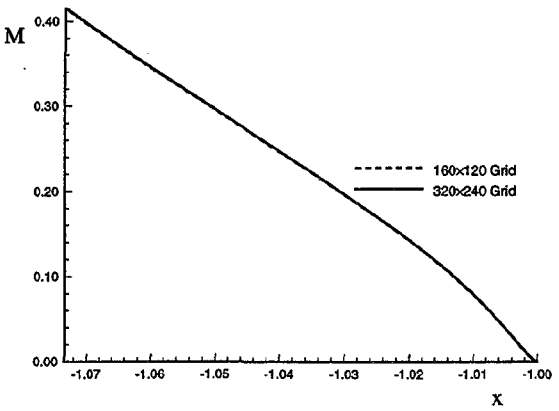

Figure 19: Comparison of steady solution of the Mach number along the stagnation line for two set of grids.

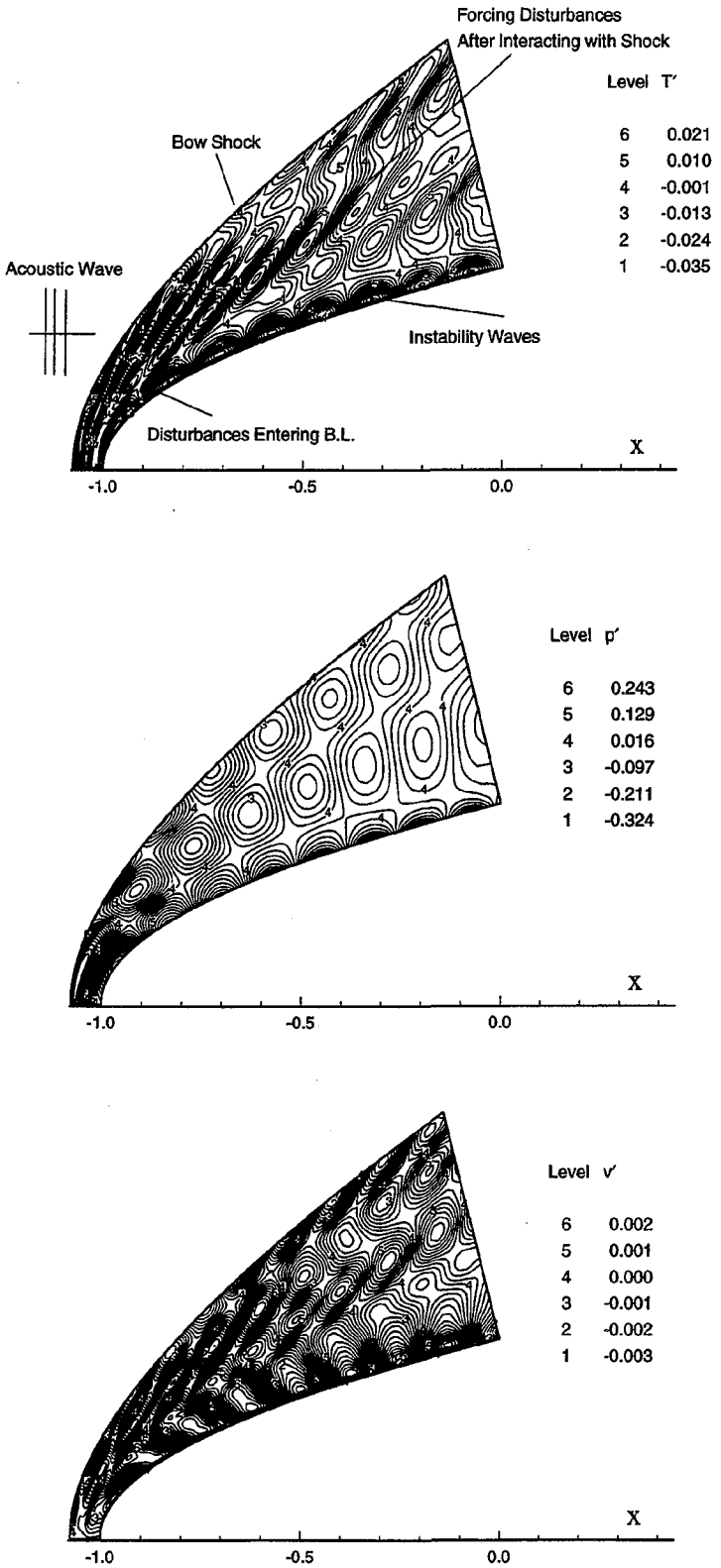

Figure 20: Instantaneous contours of perturbations of flow variables: temperature (upper figure), pressure (middle figure), and velocity component in y direction (lower figure).

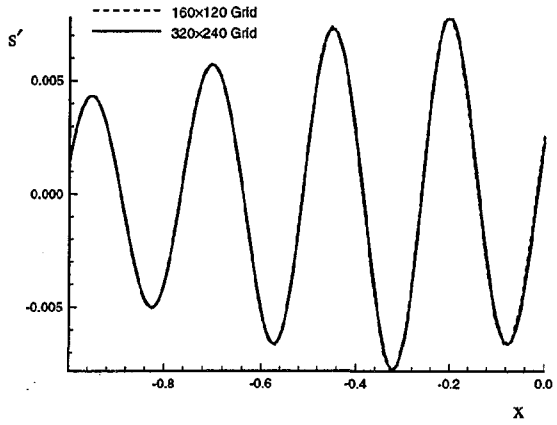

Figure 21: Distribution of instantaneous entropy perturbations along the parabola surface.

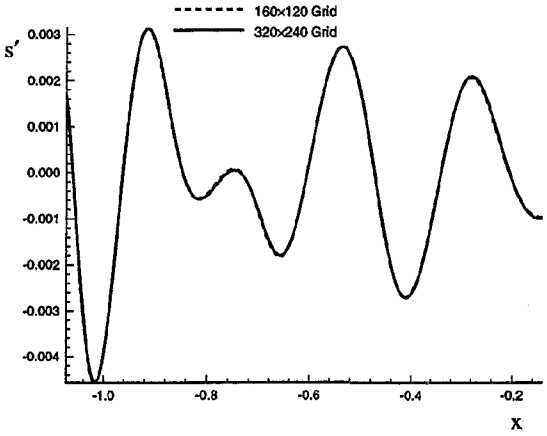

Figure 22: Distribution of instantaneous entropy perturbations immediately behind the bow shock.

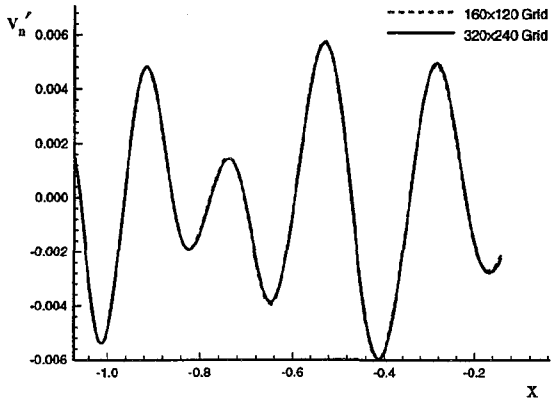

Figure 23: Instantaneous normal bow shock velocities vs. the shock x coordinates.

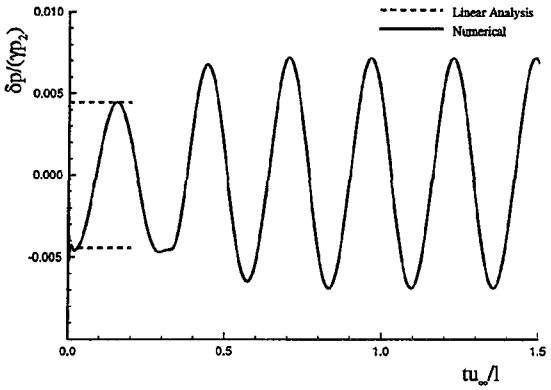

Figure 24: Time history of the instantaneous pressure perturbation at the point immediately behind the bow shock at the center line.

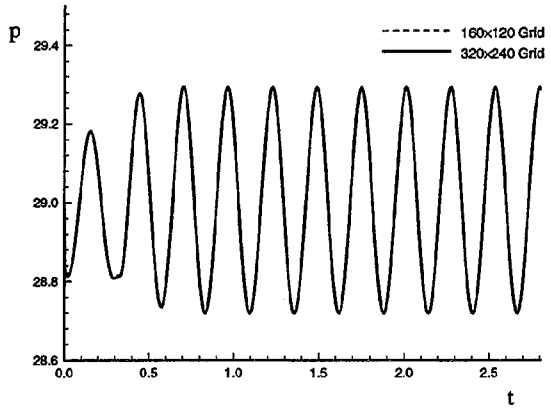

Figure 25: Comparison of the time history of the instantaneous pressure perturbation at the point immediately behind the bow shock at the center line.